The Astrophysical Journal, 969:146 (18pp), 2024 July 10 https://doi.org/10.3847/1538-4357/ad463f

A Possibly Short GRB 180418A and Phenomenology of Reverse-Shock Emission in the Optical Afterglows of Gamma-Ray Bursts

Xiang-Gao Wang[1,2], Ji-Wang Zhou[1,2], Zi-Min Zhou[1,2], WeiKang Zheng[3], Shuang-Xi Yi[4], Liang-Jun Chen[1,2], Yi-Ning Wei[1,2], Da-Bin Lin[1,2], En-Wei Liang[1,2], and Alexei V. Filippenko[3]

[1] Guangxi Key Laboratory for Relativistic Astrophysics, School of Physical Science and Technology, Guangxi University, Nanning 530004, People's Republic of China; wangxg@gxu.edu.cn
[2] GXU-NAOC Center for Astrophysics and Space Sciences, Nanning 530004, People's Republic of China
[3] Department of Astronomy, University of California, Berkeley, CA 94720-3411, USA; weikang@berkeley.edu, afilippenko@berkeley.edu
[4] School of Physics and Physical Engineering, Qufu Normal University, Qufu 273165, People's Republic of China; yisx2015@qfnu.edu.cn
Received 2023 October 4; revised 2024 April 10; accepted 2024 April 26; published 2024 July 9

Abstract

We present early-time ground-based optical follow-up observations of GRB 180418A, which was discovered by both Swift/BAT and Fermi/GBM. Its broadband afterglow was well monitored by Swift/XRT and ground-based optical telescopes. The optical light curve of GRB 180418A can be modeled by forward shock (FS) plus reverse shock (RS). We fit the light curves with standard external shock models and derive the physical properties of the outflow. It is found that the ratio $R_B \equiv \varepsilon_{B,r}/\varepsilon_{B,f}$ is 11.22, indicating a moderate degree of magnetization in the RS region. The reported duration of GRB 180418A, T_{90}, lies in the intermediate region between short and long gamma-ray bursts (GRBs). We further discuss the classification of GRB 180418A, and calculate $\varepsilon = E_{\gamma,\mathrm{iso},52}/E_{p,z,2}$ values of 0.026 and 0.018 (assuming the redshift z is 1.0 and 1.5, respectively), which is closer to short GRBs (SGRBs) in the ε-$T_{90,z}$ plane. If GRB 180418A is an SGRB, it is the only reported SGRB thus far with RS emission in optical light curves. In order to compare the properties of GRB 180418A, we collected three SGRBs that may have RS emission (GRBs 060313, 090426, and 210207B) and also 22 long GRBs (LGRBs) with RS emission. We find that the parameters of LGRBs are in a wider range than those of SGRBs. Also, SGRBs appear to have very small R_B values, but the results are generally similar to those of LGRBs. The fitting parameters of GRB 180418A are generally consistent with those of the other three SGRBs, implying that GRB 180418A may belong to the category of SGRBs.

Unified Astronomy Thesaurus concepts: Gamma-ray bursts (629)

1. Introduction

Gamma-ray bursts (GRBs) are among the most energetic events in the Universe. There are two populations: short GRBs (SGRBs) and long GRBs (LGRBs), based on their distribution of the T_{90} duration (the time interval between the epochs when 5% and 95% of the total fluence is collected by the detector), which includes at least two Gaussian components in logarithmic space with a separation of ∼2 s in the observer frame (Kouveliotou et al. 1993). There are other secondary parameters, such as hardness and spectral lag (Kumar & Zhang 2015) to further support the classification. It is generally believed that most LGRBs arise from the core collapse of massive stars (Woosley 1993; Hjorth et al. 2003) and are associated with hydrogen-poor, high-velocity Type Ic supernovae (SNe Ic Wang et al. 2007; Cano 2013). In contrast, SGRBs are thought to be the consequence of mergers of compact objects driven by angular momentum and energy losses to gravitational radiation; the merger system can be a neutron star–neutron star (NS–NS) or neutron star–black hole (NS–BH; Eichler et al. 1989; Paczynski 1991; Narayan et al. 1992; Ruffert & Janka 1998; Rosswog & Ramirez-Ruiz 2002; Lee & Ramirez-Ruiz 2007; Giacomazzo et al. 2011). On 2017 August 17, an NS–NS merger event (GW170817) was detected by the Advanced LIGO and Advanced Virgo gravitational-wave detectors (Abbott et al. 2017), which was accompanied by the short GRB 170817A, thus confirming that NS–NS mergers can produce SGRBs. This proves that at least some SGRBs originate from mergers of compact objects.

Nevertheless, there is some overlap between the distributions of T_{90} and hardness among the two populations of GRBs, and in some cases it is unclear whether a burst with intermediate properties belongs to the population of SGRBs or LGRBs. The relative significance of the two components and the peak duration values depend on energy and sensitivity (Kouveliotou et al. 1993; Sakamoto et al. 2008; Paciesas & Fermi GBM Collaboration 2012; Zhang et al. 2012; Qin et al. 2013). It has also been reported that some peculiar short-duration GRBs but with long active tails, such as GRB 200826A (Zhang et al. 2021), originate from massive-star core collapse. Thus, a new classification method was proposed, namely compact-star origin (Type I) and massive-star origin (Type II; Zhang et al. 2009; Lü et al. 2010; Wang et al. 2015).

Two distinct emission phases occur in the GRB fireball scenario. First, there is a prompt phase producing gamma-ray radiation through internal shocks within the relativistic jet that dissipates its internal kinetic energy. Then, there is an afterglow phase during which longer, fading, multiwavelength emission is radiated from the external shocks between the jet and the circumstellar medium (Piran 1999; Kumar & Zhang 2015). Two kinds of external shocks are important: the long-duration forward shock (FS), which propagates outward, sweeping up the circumstellar medium, and the short-lived reverse shock (RS), which propagates backward into the jet (Meszaros & Rees 1993). Emission from the FS can explain the afterglow

phase of many GRBs, and the dynamics of the FS have been amply explored (Mészáros & Rees 1997; Sari & Piran 1999a; Granot & Sari 2002). On the other hand, RS emission is useful for understanding the initial bulk Lorentz factor, the ejecta composition, and magnetization (Steele et al. 2009; Mundell et al. 2013; Fraija et al. 2016; Fraija et al. 2019; Fraija 2014). Since RS emission was first detected in GRB 990123 (Akerlof et al. 1999), extensive studies of RS emission in optical and infrared bands have been made with early-time afterglow data (Mészáros & Rees 1999; Sari & Piran 1999b; Fan et al. 2002; Kobayashi & Zhang 2003; Kumar & Panaitescu 2003; Zhang et al. 2003; Fan et al. 2004; Nakar & Piran 2004; Zhang & Kobayashi 2005; Zou et al. 2005; Harrison & Kobayashi 2013; Yi et al. 2013; Japelj et al. 2014; Gao et al. 2015; Zhang et al. 2015; Yi et al. 2020). Motivated by the extremely bright RS emission detected in GRB 990123, it is expected that the Swift Ultraviolet and Optical Telescope (UVOT) and ground-based rapid follow-up optical telescopes can detect RS emission in a large sample of GRBs (Zhang et al. 2003).

In this work, we present multiwavelength afterglow monitoring of the potentially short GRB 180418A, mainly from observations with the 0.76 m Katzman Automatic Imaging Telescope (KAIT; Filippenko et al. 2001) at Lick Observatory starting 155 s after the trigger and find that the early-time optical afterglow of GRB 180418A can be attributed to reverse-shock (RS) emission. We also discuss the possibility that GRB 180418A is an SGRB. Moreover, we collect three other SGRBs (GRBs 060313, 090426, and 210207B) that may have RS emission, as well as 22 LGRBs that have reported RS emission, and compar their parameters.

The paper is organized as follows. Section 2 presents the ground-based optical follow-up observations of GRB 180418A, along with the temporal and spectral analysis of the afterglow. We fit the optical light curve of GRB 180418A with RS + FS models and also derive their physical parameters. In Section 3, we collect three SGRBs and 22 LGRBs having RS emission, and applied a Markov Chain Monte Carlo (MCMC) algorithm to match the observed light curves. Our discussion and conclusions are presented in Section 4. Throughout the paper, temporal and spectral slopes are defined as $F \propto t^{\alpha}\nu^{\beta}$, and the notation $Q_n = Q/10^n$ in cgs units is adopted.

2. GRB180418A

2.1. Observations

The Swift/BAT[5] instrument triggered on GRB 180418A (trigger #826428) at T_0 of 2018 March 25, 06:44:06.012 (UTC dates are used herein). The Swift/BAT light curve showed a single FRED-like (fast rise, exponential decay) with a duration of $T_{90} = 1.5$ s (D'Elia et al. 2018). T_{90} was reported as 4.408 s (50–300 keV)[6] and other values (Palmer et al. 2018; Becerra et al. 2019).

The object was also detected by the Gamma-Ray Burst Monitor (GBM) onboard the Fermi satellite[7] at 06:44:06.28 (trigger #545726651/180418281), again showing a single FRED-like peak with $T_{90} \approx 2.5$ s (50–300 keV) (Bissaldi & Veres 2018). Rouco Escorial et al. (2021) reanalyzed the value of T_{90} for GRB 180418A, and obtained 1.90 ± 0.76 s (16 ms bin) and 2.56 ± 0.29 s for Swift/BAT and Fermi/GBM, respectively. The X-ray Telescope (XRT) onboard Swift began observing the X-ray afterglow of GRB 180418A at 3179 s after the Swift/BAT trigger (Osborne et al. 2018).

Dozens of ground-based optical telescopes observed the afterglow of GRB 180418A (Zheng & Filippenko 2018; Guidorzi et al. 2018; Troja et al. 2018a; Sota et al. 2018; Fong et al. 2018; Malesani et al. 2018; Xin et al. 2018; Misra et al. 2018; Troja et al. 2018b; Schady & Chen 2018; Choi et al. 2018; Horiuchi et al. 2018; Klotz et al. 2018; Bright et al. 2018). KAIT at Lick Observatory responded automatically and began imaging the field at 06:46:41 UTC, 155 s after the burst. Observations were performed with an automatic sequence in the clear (roughly R), V, and I filters, and the exposure time was 20 s per image (Zheng & Filippenko 2018). Our photometry is reported in Table 1. In order to study the continuous light-curve behavior of GRB 180418A, we also adopted published photometry from the literature (Becerra et al. 2019; Rouco Escorial et al. 2021). Since most optical data are in the R and r bands, we first calibrate the data from r to R with the expression $m_R = m_r - 2.5\beta_O \log_{10}(\lambda_R/\lambda_r) + 2.5\log_{10}(f_{0,R}/f_{0,r})$, where $\beta_O = 0.76$ (see Section 2.2), and then convert the R magnitudes to flux density in units of μJy with the expression $F_R = \lambda_R 10^{(\log_{10}(f_{o,R}) - 0.4m_R)}$, where λ_R is the mean wavelength in the R band. In addition, the Swift/XRT data were extracted from the UK Swift Science Data Center at the University of Leicester (Evans et al. 2009).[8] Figure 1 shows the light curves of the afterglow in optical and X-ray bands.

2.2. Temporal and Spectral Behavior of the Afterglow

In order to obtain the temporal profile of the afterglow, we employed a single-power-law (SPL) function (e.g., Liang et al. 2008; Pozanenko et al. 2013; Wang et al. 2015),

$$F = F_0 t^{-\alpha}, \tag{1}$$

where F_0 is the flux normalization and α is the afterglow flux decay index, as well as a broken-power-law (BPL) function,

$$F = F_1\left[\left(\frac{t}{t_b}\right)^{\omega\alpha_1} + \left(\frac{t}{t_b}\right)^{\omega\alpha_2}\right]^{-1/\omega}, \tag{2}$$

where F_1 is the flux normalization, α_1 and α_2 are respectively the afterglow flux decay indices before and after the break time (t_b), and ω is a smoothness parameter which represents the sharpness of the break. The X-ray light curve (starting ~3000 s after the BAT trigger as shown in Figure 1) can be fitted with an SPL function having decay index $\alpha_X = -1.0 \pm 0.06$. The temporal index α_X is expected to be related to the electron energy index p by $\alpha_X = 3(p-1)/4$; hence, one can predict $p = 2.33 \pm 0.06$, where p is the index of the synchrotron radiating electron spectrum $N_e \propto \gamma_e^{-p}$.

A clear bump appeared in the optical light curve at early times, and we used a BPL function to fit it, giving rising and decaying slopes of $\alpha_{O,I} = 2.50$ (fixed) and $\alpha_{O,II} = -2.02 \pm 0.20$, respectively, and a peak time of $t_{peak} = 37.13 \pm 1.33$ s. At $t \gtrsim 500$ s, the light curve is dominated by another smooth BPL

[5] Swift is a multiwavelength observatory for studies of GRBs; the gamma-ray Burst Alert Telescope (BAT) detects GRBs and accurately determines their position in the sky.

[6] Reported in the official BAT catalog later (https://swift.gsfc.nasa.gov/results/batgrbcat/GRB180418A/ web/GRB180418A.html), calculated using the standard setup of the BAT pipeline with a bin size of 4~ms (batgrbproduct; Lien et al. 2016).

[7] The Fermi Gamma-ray Space Telescope is an international space mission that studies the cosmos in the energy range 10 keV–300 GeV.

[8] https://www.swift.ac.uk/xrt_curves/00826428/

Table 1
KAIT Photometry Log of GRB 180418A

$T - T_0$(mid, s)	Exp (s)	Mag	Err (1σ)	Filter
165	10	16.17	0.04	*Clear*
267	10	16.99	0.04	*Clear*
367	10	17.35	0.07	*Clear*
467	10	17.55	0.07	*Clear*
570	10	17.83	0.12	*Clear*
670	10	17.94	0.13	*Clear*
770	10	18.31	0.19	*Clear*
870	10	18.27	0.15	*Clear*
972	10	18.52	0.17	*Clear*
1072	10	18.33	0.09	*Clear*
1172	10	18.47	0.14	*Clear*
1276	10	18.55	0.10	*Clear*
1373	10	18.61	0.14	*Clear*
1473	10	18.72	0.07	*Clear*
1575	10	18.82	0.12	*Clear*
1641	10	18.85	0.10	*Clear*
1708	10	18.76	0.07	*Clear*
1775	10	18.68	0.06	*Clear*
1841	10	18.89	0.09	*Clear*
1911	10	18.79	0.06	*Clear*
1977	10	18.88	0.06	*Clear*
2044	10	18.98	0.09	*Clear*
2111	10	19.03	0.09	*Clear*
2175	10	19.19	0.12	*Clear*
2245	10	19.18	0.11	*Clear*
2311	10	19.40	0.14	*Clear*
2376	10	19.09	0.09	*Clear*
2442	10	19.33	0.12	*Clear*
2509	10	19.18	0.12	*Clear*
2581	10	19.37	0.14	*Clear*
2647	10	19.46	0.16	*Clear*
2714	10	19.36	0.11	*Clear*
2741	10	19.49	0.14	*Clear*
2997	30	19.32	0.09	*Clear*
3224	30	19.49	0.13	*Clear*
3450	30	19.46	0.14	*Clear*
3677	30	19.62	0.13	*Clear*
3903	30	19.65	0.12	*Clear*
4129	30	19.68	0.16	*Clear*
4362	90	19.89	0.14	*Clear*
5037	90	19.60	0.23	*Clear*
232	10	16.27	0.15	*I*
333	10	17.16	0.28	*I*
433	50	17.38	0.13	*I*
940	50	18.70	0.36	*I*
1440	90	18.52	0.08	*I*
2077	100	18.92	0.10	*I*
2922	270	19.44	0.13	*I*
198	10	16.72	0.17	*V*
300	10	17.53	0.23	*V*
400	30	18.13	0.21	*V*
704	40	18.41	0.20	*V*
1105	50	19.21	0.22	*V*
2846	240	20.40	0.23	*V*

component from the FS, and the decay slope at late epochs is fixed to be 1.0, typical for FS decay at late times(Gao et al. 2015). The fitting results are shown in Figure 1. In the framework of the RS model for an interstellar medium (ISM) scenario, depending on the relative strength and peak times of the RS and FS afterglow components, four different light-curve configurations are expected to be observed (Zhang et al. 2003; Gomboc et al. 2009; Gao et al. 2015), and GRB 180418A

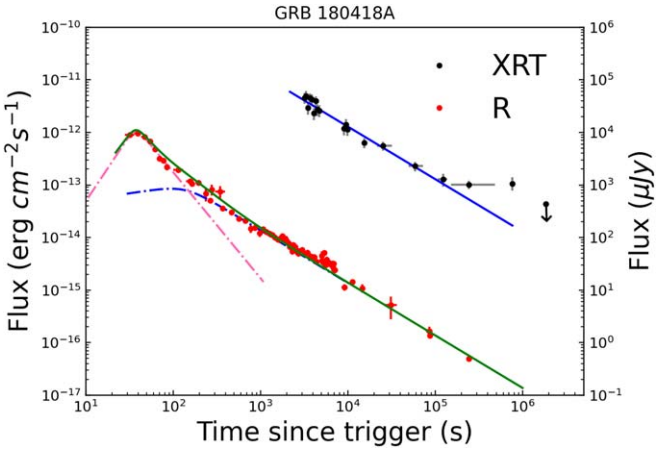

Figure 1. Optical and X-ray afterglow light curves of GRB 180418A with our empirical fits. The optical light curve shows a bump at early times, which rises with an index of $\alpha_{O,I} = 2.50$ (fixed). and then decays with an index of $\alpha_{O,II} = -2.02 \pm 0.20$ (pink dotted line). At $t \gtrsim 500$ s, the decay slope is fixed to be 1.0 (blue dotted line).

agrees with that of the RS II type in the thin-shell case defined by Gao et al. (2015): light curves with characteristic flattening due to a bright RS afterglow outshining the FS emission. (Note that RS I light curves show prominent RS and FS afterglow peaks.) The expected RS emission light curve increases as $F \propto t^5$ and decays roughly as t^{-2} after the peak for the thin-shell case. For GRB 180418A, the observed decay slope of the early bump is -2 ± 0.20, consistent with the expected value of $\alpha^{\rm d}_{\rm ISM} = -(27p + 7)/35 \approx -2.0$ when $p = 2.33$. For the rising slope, the observed value of 2.50 is shallower than the expectation of the RS II type ($\alpha^{\rm r}_{\rm ISM} = (6p - 3)/2 = 5.49$ when $p = 2.33$). However, considering that there is only one data point prior to the peak, and it may be contaminated by prompt optical emission, the rising index could in fact be steeper than what was observed; thus, we consider the observed value to be in agreement with the RS II type.

We also analyzed the spectral energy distribution (SED) of the GRB 180418A afterglow by jointly fitting the optical and Swift/XRT data with the *Xspec* package (Arnaud 1996). Data in the time interval 3091–4831 s are used. The Swift/XRT data are corrected for photoelectric absorption of hydrogen in the Milky Way and fitted for the host galaxy: the equivalent hydrogen column density of the Milky Way is fixed to be $N_{\rm H} = 1.07 \times 10^{20}$ cm^{-2}, while for the host galaxy, $N_{\rm H}^{\rm host} = (6.67 \pm 8.41) \times 10^{20}$ cm^{-2} is derived from the fitting. Similarly, for the optical extinction, we fix the Milky Way component to be $E(B - V) = 0.017$ mag, and we fit the host-galaxy component assuming a Small Magellanic Cloud (SMC) extinction law with $R_{V,\rm SMC} = 2.93$ (Pei 1992). The host-galaxy extinction is found to be almost negligible, with $E(B - V) < 0.001$ mag.

The results of the SED fitting are shown in Figure 2. The SED of the joint optical and X-ray spectrum can be well fitted with an SPL function having photon index $\Gamma = 1.76 \pm 0.08$, which means that the emission in the optical and X-ray bands may have the same origin, and $\beta = \Gamma - 1 = 0.76 \pm 0.08$.

Our analysis is consistent with that of Becerra et al. (2019), who adopted a similar RS plus FS model and a constant-ISM scenario in the thin-shell case; they also found similar values for p (2.35 ± 0.01) and β (0.73 ± 0.03). A similar conclusion was also reached by Rouco Escorial et al. (2021).

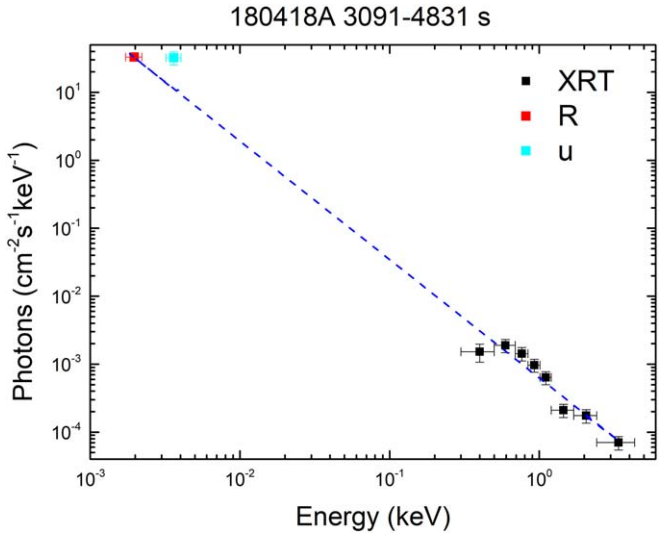

Figure 2. SED of the GRB 180418A afterglow from X-ray to optical bands in the time interval 3091–4831 s. The dashed line shows the intrinsic power-law spectra derived from the joint fits, with $\Gamma = 1.76 \pm 0.08$. The u band from Swift/UVOT is designated u.

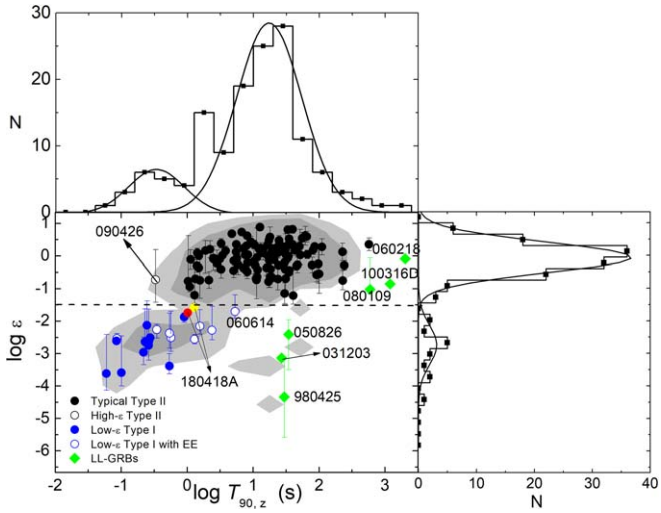

Figure 3. Comparison of GRB 180418A with other GRBs in the ε–$T_{90,z}$ plane. The yellow and red dots are the positions of GRB 180418A when assuming $z = 1.0$ and $z = 1.5$, respectively. GRB 180418A appears to be closer to the SGRB region.

2.3. Classification of GRB 180418A

The classification of GRB 180418A remains ambiguous because its properties lie between those of SGRBs and LGRBs. Becerra et al. (2019) used spectral hardness and spectral lag methods to classify it and considered that GRB 180418A has a certain probability (10%–30%) to be an SGRB. Rouco Escorial et al. (2021) calculated the γ-ray fluence ($f_\gamma = 2.85 \pm 0.20 \times 10^{-7}$ erg cm^{-2} in the 15–350 keV range) and hardness ratio (f_γ(50–100 keV)/f_γ(25–50 keV) = 1.47) of GRB 180418A, which seem to be close to the boundary between short and long GRBs. They in addition compared the parameters of GRB 180418A with those of the Fermi/GBM catalog comprising 1405 GRBs, and used the Hardness–T_{90} plane to conclude that GRB 180418A is likely a short-hard GRB.

Here, we expand the discussion of whether GRB 180418A is an SGRB or an LGRB. Lü et al. (2010) proposed using the ε–$T_{90,z}$ distribution to distinguish between Type I and Type II GRBs, where $T_{90,z} = T_{90}/(1+z)$ and z is the redshift. The parameter $\varepsilon = E_{\gamma,\mathrm{iso},52}/E_{p,z,2}$, where $E_{\gamma,\mathrm{iso},52} = E_{\gamma,\mathrm{iso}}/10^{52}$ ($E_{\gamma,\mathrm{iso}}$is the burst isotropic gamma-ray energy) and $E_{p,z,2} = E_p/(100\,\mathrm{keV})$ (E_p is the rest-frame spectral peak energy). For GRB 180418A, Rouco Escorial et al. (2021) calculated that $E_{\mathrm{peak}} = 329 \pm 123$ keV, and they also found $E_{\gamma,\mathrm{iso}}$ values of 2.71×10^{51} erg and 5.95×10^{51} erg when the redshift is 1.0 and 1.5, respectively. $T_{90} = 2.56$ (Rouco Escorial et al. 2021) is adopted in our analysis. We obtained the value of ε, $\varepsilon = 0.026$, and $\varepsilon = 0.018$ for $z = 1$ and $z = 1.5$, respectively. We also compare the values of GRB 180418A with those of GRBs collected by Lü et al. (2010). Figure 3 shows the position of GRB 180418A in the ε–$T_{90,z}$ plane, indicating that GRB 180418A is closer to the SGRB region.

Amati et al. (2002) discovered a correlation between the GRB isotropic bolometric emission energy, $E_{\gamma,\mathrm{iso}}$, and the rest-frame peak energy, $E_{p,z} = (1+z)E_{p,z}$ Rouco Escorial et al. (2021). find that GRB 180418A lies closer to the Amati correlation followed by the SGRB population. Wang et al. (2018) use the Type II GRB samples that they collect to fit a tight Amati relation, but Type I GRBs generally deviate from this relation with a relatively low energy and high $E_{p,z}$. Figure 4

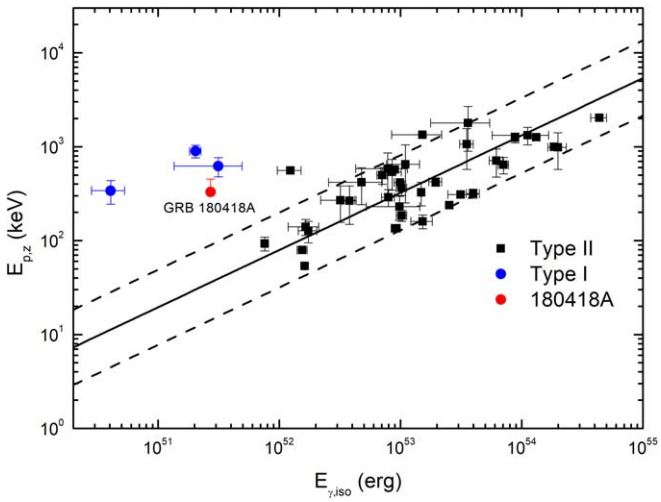

Figure 4. The Amati relation, with 2σ dispersion regions shown with dashed lines; the red dot is the position of GRB 180418A when assuming $z = 1.0$.

shows the position of GRB 180418A in the $E_{\gamma,\mathrm{iso}}$–$E_{p,z}$ plane (Amati relation), where GRB 180418A is outside of the 2σ dispersion regions (shown with the dashed lines). Therefore, GRB 180418A likely belongs to Type I, namely the compact-star type.

In summary, our above analysis is in favor of GRB 180418A being an SGRB, similar to the conclusion suggested by both Becerra et al. (2019) and Rouco Escorial et al. (2021).

2.4. Model Fit

The analysis in Section 2.2 suggests that the optical afterglow may be attributed to RS and FS emission from external shocks in the constant-ISM scenario. Synchrotron emission is expected behind both shocks. In this case, the typical synchrotron frequency, ν_m, is below the cooling synchrotron frequency, ν_c, and the spectrum is composed of three power-law segments: $F_\nu \propto \nu^{1/3}$, $\nu^{-(p-1)/2}$, and $\nu^{-p/2}$, joined at break frequencies ν_m and ν_c (Sari et al. 1998). The decaying slope of the RS emission of GRB 180418A agrees

with that of the RS II type in the thin-shell case; thus, we also assumed that the thin-shell scenario applies to our analysis. Because we are primarily interested in optical wavelengths, we ignore synchrotron self-absorption.

At redshift z and frequency ν, the model light curve is determined by a set of parameters,

$$F_{t,\nu,\rm obs} = f\,(t,\,\nu;\,E_{\rm k,iso},\,\Gamma_0,\,n,\,\varepsilon_{e,r},\,\varepsilon_{B,r},\,\varepsilon_{e,f},\,\varepsilon_{B,f},\,p,\,\theta_{\rm j}), \quad (3)$$

where n is the density of the circumburst ISM, $E_{\rm k,iso}$ is the isotropic kinetic energy of the fireball, Γ_0 is the initial fireball Lorentz factor, $\theta_{\rm j}$ is the jet opening angle, p is the electron spectral index, and the fractions of internal energy to the electrons and magnetic field are (respectively) $\varepsilon_{e,r}$ and $\varepsilon_{B,r}$ in the RS region and $\varepsilon_{e,f}$ and $\varepsilon_{B,f}$ in the FS region. We also take the redshift of GRB 180418A to be a typical value of 1.0. Our goal is to compare a theoretical model to the observed light curve. The free model parameters include $\varepsilon_{e,r}$, $\varepsilon_{B,r}$, $\varepsilon_{e,f}$, $\varepsilon_{B,f}$, n, Γ_0, $\theta_{\rm j}$, $E_{\rm k,iso}$, and p. A more detailed description of the FS model is given by Sari et al. (1998); Huang et al. (2000), and Fan & Piran (2006), while a thorough description of the RS model can be found in Yi et al. (2013, 2020) and Gao et al. (2015).

Here we present our fits to the X-ray and optical afterglow light curves with the standard external shock models. We assume that the spectrum of radiating electrons is $N_e \propto \gamma_e^{-p}$. With the observed spectral index and temporal decay slope of the normal decay segment, we also suggest that both the optical and X-ray emission should be in the spectral regime between ν_m and ν_c, and roughly take $p = 2.33$. Our empirical analysis shows that the rising and decaying slopes of the RS emission are consistent with expectations in the ISM scenario. We then adopt a constant medium density (n). The temporal evolution of both the minimum and cooling frequencies (ν_m and ν_c) in the RS and FS regions are taken from Yost et al. (2003); Fan & Piran (2006); Zhang et al. (2007a), and Yi et al. (2013). The model does not incorporate emission produced by the inverse-Compton effect, which is expected to delay the transition between the fast and slow cooling phases, as well as to decrease the cooling frequency in the FS (Wu et al. 2005).

We used the MCMC algorithm available in the Python package `emcee` (Foreman-Mackey et al. 2013) with 90 walkers running for 10,000 steps in each circle to make the best fit to the observed light curves. In the MCMC sampling process, the log-likelihood function is given by (e.g., Ren et al. 2019)

$$\ln \mathcal{L} = \frac{1}{M}\sum_{i}^{M} \ln \mathcal{L}_i, \quad (4)$$

where M is the number of wavelengths (in our case $M = 2$ for the R band and X-rays), and $\ln \mathcal{L}_i$ is the Gaussian likelihood for the data in band i, which is simply given by (e.g., D'Agostini 2005; Ivezić et al. 2014),

$$\ln \mathcal{L}_i = -\frac{1}{2}\sum_{j} \frac{(O_{i,j} - O_{i,j}^{\rm mod})^2}{\sigma_{i,j}^2}, \quad (5)$$

where $O_{i,j}$, $O_{i,j}^{mod}$ and $\sigma_{i,j}$ are the jth observed flux density, model flux density, and observed uncertainties, respectively. To evaluate the goodness of modeling, the reduced chi-squared $\chi^2_{\rm dof}$ (e.g., D'Agostini 2005; Ivezić et al. 2014; Yang et al. 2022),

$$\chi^2_{\rm dof} = \frac{\chi^2}{\rm dof} = -\frac{2}{\rm dof}\ln \mathcal{L}, \quad (6)$$

is used, where dof is the number of fitting degrees of freedom.

The preliminary parameters are set in the following ranges: $\log_{10}(E_{\rm k,iso}/{\rm erg}) \in [50.00,\ 56.00]$, $\log_{10}\Gamma_0 \in [1.00,\ 3.00]$, $\log_{10}(n/{\rm cm^{-3}}) \in [-3.00,\ 3.00]$, $p \in [2.00,\ 3.50]$, $\log_{10}\varepsilon_{B,f} \in [-8.00,\ -0.5]$, $\log_{10}\varepsilon_{e,f} \in [-5.00,\ -0.10]$, $\log_{10}\varepsilon_{B,r} \in [-6.00,\ -0.5]$, $\log_{10}\varepsilon_{e,r} \in [-5.00, -0.10]$, and $\theta_{\rm j}(^\circ) \in [1.00,\ 20.00]$. We found that the standard external shock models can fit the light curves well by considering both RS and FS emission. A set of optimum parameters was obtained in our MCMC results, with $\log_{10}(E_{\rm k,iso}/{\rm erg}) = 52.09^{+0.22}_{-0.15}$, $\log_{10}\Gamma_0 = 2.08^{+0.10}_{-0.07}$, $\log_{10}(n/{\rm cm^{-3}}) = 0.74^{+0.46}_{-0.59}$, $p = 2.34^{+0.03}_{-0.03}$, $\log_{10}\varepsilon_{B,f} = -2.77^{+0.31}_{-0.27}$, $\log_{10}\varepsilon_{e,f} = -1.51^{+0.11}_{-0.14}$, $\log_{10}\varepsilon_{B,r} = -1.72^{+0.35}_{-0.27}$, $\log_{10}\varepsilon_{e,r} = -1.37^{+0.13}_{-0.18}$, and $\theta_{\rm j}(^\circ) = 11.29^{+1.20}_{-1.50}$ for GRB 180418A (as reported in Table 2 and shown in Figure 5). We also calculated the radiation efficiency of GRB 180418A, $\eta = E_{\gamma,\rm iso}/(E_{\rm k,iso} + E_{\gamma,\rm iso}) \approx 0.18$. The derived efficiencies are consistent with previous results (e.g., Wang et al. 2015; Beniamini et al. 2016; Zhang et al. 2007b).

Gao et al. (2015) reported that typical GRBs usually have an $\varepsilon_{B,f}$ value in the range of $[10^{-2}$–$10^{-6}]$. We derive $\varepsilon_{B,f} = 10^{-1.72^{+0.46}_{-0.59}}$. The value of $\varepsilon_{B,f}$ for GRB 180418A is consistent with the range provided by Gao et al. (2015), including the uncertainty. Fan et al. (2002) proposed that the magnetization parameter of the RS and FS regions should be different, according to the model parameters of both RS and FS emission from GRB 990123 (Panaitescu & Kumar 2001a). Defining the magnetization parameter $R_B \equiv \varepsilon_{B,r}/\varepsilon_{B,f}$, we get $R_B \approx 11.22$ for GRB 180418A. Note that the estimated R_B values are dramatically different among GRBs (Japelj et al. 2014; Gao et al. 2015; Yi et al. 2020). The R_B value of GRB 180418A derived in our analysis is at the low end of the range obtained by Japelj et al. (2014), indicating a moderate magnetization in the RS region. The ratio $R_e \equiv \varepsilon_{e,r}/\varepsilon_{e,f}$ may indicate the relative radiation efficiency of the RS to the FS. We obtain $R_e \equiv \varepsilon_{e,r}/\varepsilon_{e,f} \approx 1.38$, implying that the radiation efficiency of the RS exceeds that of the FS.

3. RS Emission of GRBs

If GRB 180418A was indeed an SGRB, it is the first SGRB with RS emission detected in the optical band (Rouco Escorial et al. 2021), and thus of great significance to understanding RS emission. RS is an important part of the afterglow; it is the result of interaction between a relativistic jet and an ambient medium. The RS component is usually too weak compared with the FS emission or completely suppressed for some reason. Also, because of the delayed response from ground-based telescopes, there are very few GRBs whose RS emission has been detected in the optical band. Moreover, all GRBs detected with optical RS emission are LGRBs; none has been reported from SGRBs.

In order to compare the properties of GRB 180418A and study the phenomenology of RS emission in optical afterglows of GRBs, we collected a sample of GRB afterglows with RS signatures including three SGRBs and 22 LGRBs and used an MCMC algorithm available in the Python package `emcee` (Foreman-Mackey et al. 2013) to fit their optical light curves with RS and FS models. Note that all of these GRBs have no

Table 2
Fitting Results of External Shock Model for SGRBs

GRB[a]	$\log_{10}(E_{k,\rm iso}/{\rm erg})$	$\log \Gamma_0$	$\log_{10}(n/{\rm cm}^{-3})$	$\log \epsilon_{B,f}$	$\log \epsilon_{e,f}$	p	$\theta_{\rm j}$ (°)	$\log \epsilon_{B,r}$	$\log \epsilon_{e,r}$	z[b]	$R_B \equiv \varepsilon_{B,r}/\varepsilon_{B,f}$	$R_e \equiv \varepsilon_{\rm e,r}/\varepsilon_{e,f}$	$\chi^2_{\rm dof}$
180418A	$52.09^{+0.22}_{-0.15}$	$2.08^{+0.10}_{-0.07}$	$0.74^{+0.46}_{-0.59}$	$-2.77^{+0.31}_{-0.27}$	$-1.51^{+0.11}_{-0.14}$	$2.34^{+0.03}_{-0.03}$	$11.29^{+1.20}_{-1.50}$	$-1.72^{+0.35}_{-0.27}$	$-1.37^{+0.13}_{-0.18}$	1.0	11.22	1.38	1.10
060313	$52.21^{+0.31}_{-0.21}$	$1.95^{+0.04}_{-0.08}$	$0.03^{+0.45}_{-0.34}$	$-4.23^{+0.17}_{-0.36}$	$-0.06^{+0.04}_{-0.15}$	$2.16^{+0.04}_{-0.04}$	$3.19^{+0.91}_{-0.63}$	$-3.30^{+0.59}_{-0.49}$	$-1.63^{+0.36}_{-0.26}$	1.0	8.51	0.11	1.56
090426	$53.75^{+0.13}_{-0.46}$	$2.11^{+0.02}_{-0.07}$	$1.95^{+0.04}_{-0.07}$	$-5.05^{+0.39}_{-0.27}$	$-1.79^{+0.16}_{-0.08}$	$2.53^{+0.02}_{-0.11}$	$9.56^{+2.70}_{-0.50}$	$-3.22^{+0.11}_{-0.44}$	$-2.48^{+0.54}_{-0.10}$	2.609	67.61	0.20	3.42
210207B	$54.11^{+0.20}_{-0.24}$	$2.14^{+0.01}_{-0.03}$	$0.78^{+0.09}_{-0.24}$	$-4.40^{+0.58}_{-0.63}$	$-1.57^{+0.20}_{-0.19}$	$2.58^{+0.01}_{-0.03}$	$2.80^{+0.15}_{-1.31}$	$-3.10^{+0.54}_{-0.29}$	$-1.64^{+0.11}_{-0.21}$	1.65	19.95	0.85	16.05

Notes.
[a] Optical light-curve data references. GRB 060313: Roming et al. (2006). GRB 090426: Xin et al. (2011). GRB 210207B: Kumar et al. (2021); Zheng et al. (2021); Strausbaugh & Cucchiara (2021); Siegel & Lien (2021); Sutaria & Ray (2021).
[b] Redshift references. GRB 090426: Levesque et al. (2009). GRB 210207B: Siegel & Lien (2021). The redshift of GRB 060313 is unknown; thus, it is set to the typical value of 1.0.

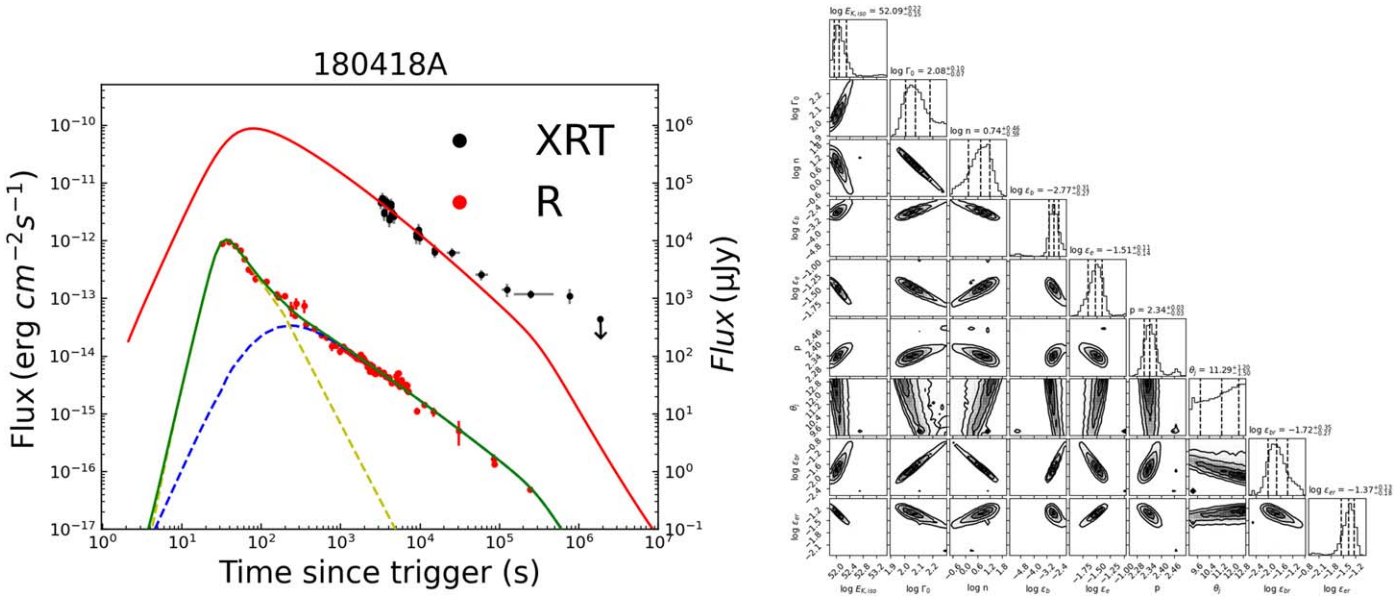

Figure 5. Left: theoretical fit to the *R*-band (green line) and X-ray (red line) afterglow light curves with RS (yellow dashed line) and FS (blue dashed line) models for GRB 180418A. Right: corner plot of the one- and two-dimensional probability distributions of the model parameters derived from our fit with the MCMC algorithm.

obvious RS emission in X-ray afterglows, so we only use the FS model to fit the X-ray light curve.

3.1. Sample Selection

The optical light curves of the GRBs were compiled from the published papers or GCN Circulars.[9] For SGRBs, we took $T_{90} \leqslant 2$ s reported in GCN Circulars or in published articles as the selection criterion. Subsequently, SGRBs were excluded if they had no optical observations before 1000 s. We finally chose three GRBs that may have RS signals: GRBs 060313, 090426, and 210207B. For LGRBs, the collection criterion was different: we collected only LGRBs having an RS component in the optical band, as reported and confirmed in articles. Japelj et al. (2014) used a parent sample of 118 GRB afterglows, with known redshift and host-galaxy extinction, to group afterglows with and without signatures of dominant RS emission and to determine which physical conditions lead to prominent RS emission, identifying 10 GRBs with RS signatures. Gao et al. (2015) made a detailed analysis of GRB early-optical afterglows, systematically investigating all Swift GRBs that have optical detections earlier than 500 s after the trigger from the launch of Swift to 2014 March. They fit the initial rising and decaying parts with a smooth BPL function and take the bursts with a decaying slope larger than 1.5 as candidates for RS light curves. Yi et al. (2020) also collected 11 GRB with early-optical light curves, which have signatures of dominant RS emission. Most of our LGRB sample is based on the above reports.

The majority of the data are collected in terms of observed magnitudes. Since most data are in the *R* band, we first calibrate the data from other wavelengths ("X" band) to the *R* band with the expression $m_R = m_x - 2.5\beta_O \log_{10}(\lambda_R/\lambda_X) + 2.5 \log_{10}(f_{0,R}/f_{0,X})$, where β_O is the optical spectral index (assuming $F_\nu \propto \nu^{-\beta_O}$ being satisfied in the optical band), and f_0 is the absolute spectral irradiance for $m = 0$ within the relevant magnitude system. An optical spectral index $\beta_O = 0.75$ is adopted when β_0 is not available (Wang et al. 2013, 2015). We then convert the *R*-band magnitudes to flux in units of μJy with the expression $F_R = \lambda_R 10^{(\log_{10}(f_{o,R}) - 0.4 m_R)}$, where λ_R is the mean wavelength in the *R* band. The Galactic extinction correction is made to the data by using a reddening map presented by Schlegel et al. (1998).

3.2. Model Fit of Samples

Following the discussion of the RS and FS models in Section 2.4, for simplicity we assume a constant-ISM environment in our modeling. Schulze et al. (2011) reveal that a constant-density ISM is a better approximation in the majority of cases according to the light curve and SED analysis of the afterglows. Japelj et al. (2014) and Gao et al. (2015) also discussed GRBs with signatures of RS emission in a constant-ISM environment. Although multiwavelength observations are routinely carried out for many GRBs and observations of radio afterglows show an RS feature in some short and long GRBs (Lloyd-Ronning & Fryer 2017; Lloyd-Ronning 2018; Lamb et al. 2019), radio-band data are still limited compared to optical and X-ray bands. Therefore, our analysis applies only to optical and X-ray data. Moreover, only upper-limit radio data are available for GRB 180418A (Bright et al. 2018). In addition, since the RS emission signal of the early-time XRT light curve was not obvious, we used only the FS model to fit the later-time data of the XRT light curve to maintain consistency with what we did for GRB 180418A in Section 2.4. But RS plus FS models are used to fit the optical light curves of all the GRBs in our sample.

We employ the MCMC algorithm to fit our SGRB and LGRB samples, using RS plus FS models at optical wavelengths and FS models in X-rays, and obtain a set of parameters determining the strengths of the RS and FS. The fitting results are reported in Figures 6–7 and Tables 2 and 3. We also calculate the magnetization parameter $R_B = \varepsilon_{B,r}/\varepsilon_{B,f}$ for SGRBs and LGRBs. Note that not all of the early-phase optical light curves can be explained using an RS plus FS model; here we discuss specific cases if additional components are needed at early times. For GRB 110205A and

[9] https://gcn.gsfc.nasa.gov/selected.html

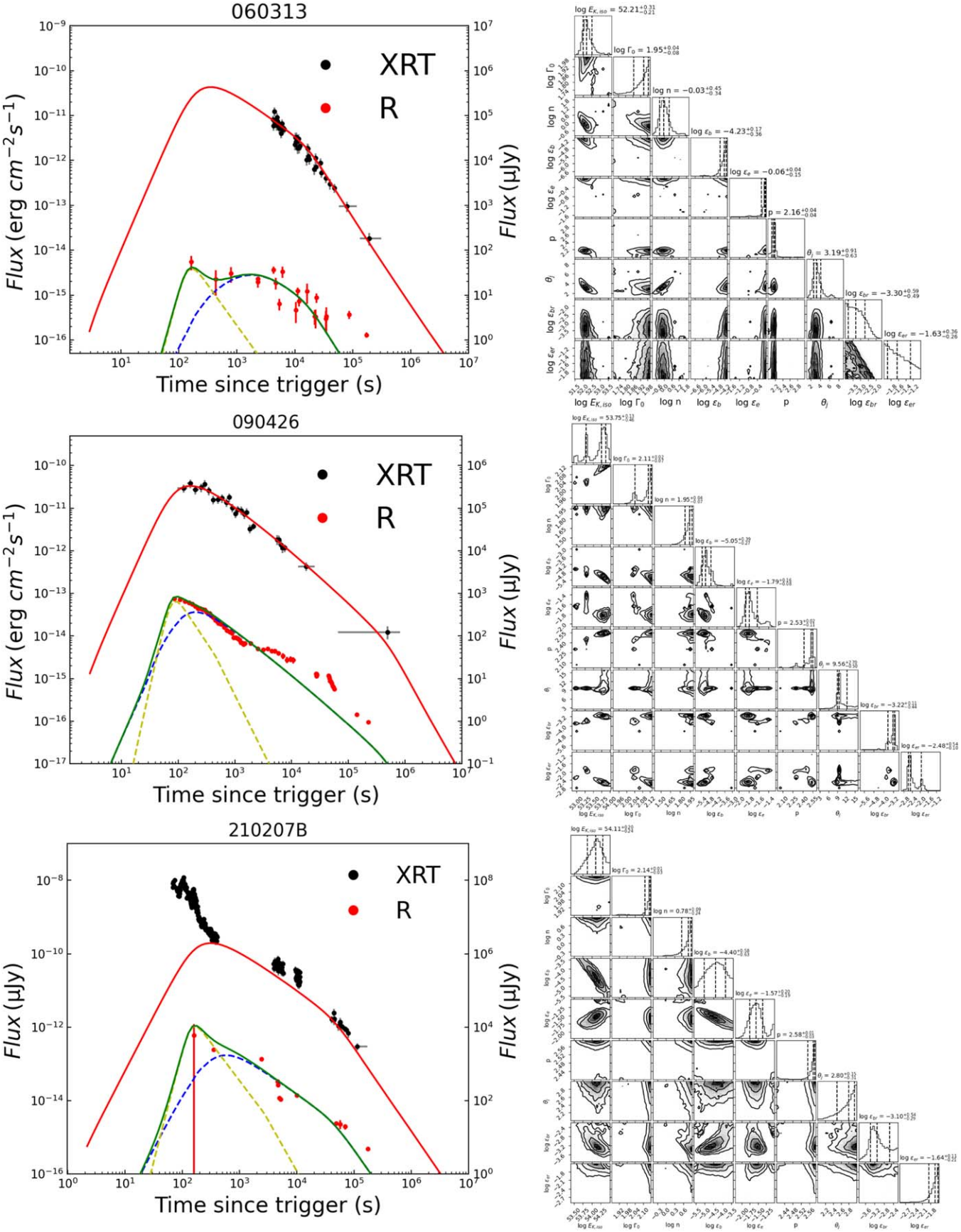

Figure 6. Left: theoretical fit with the MCMC algorithm to the *R*-band afterglow light curves with RS plus FS models and X-ray afterglow light curves with FS models for the sample of three SGRBs. Right: corner plot of the one- and two-dimensional probability distributions of the model parameters derived from our fit.

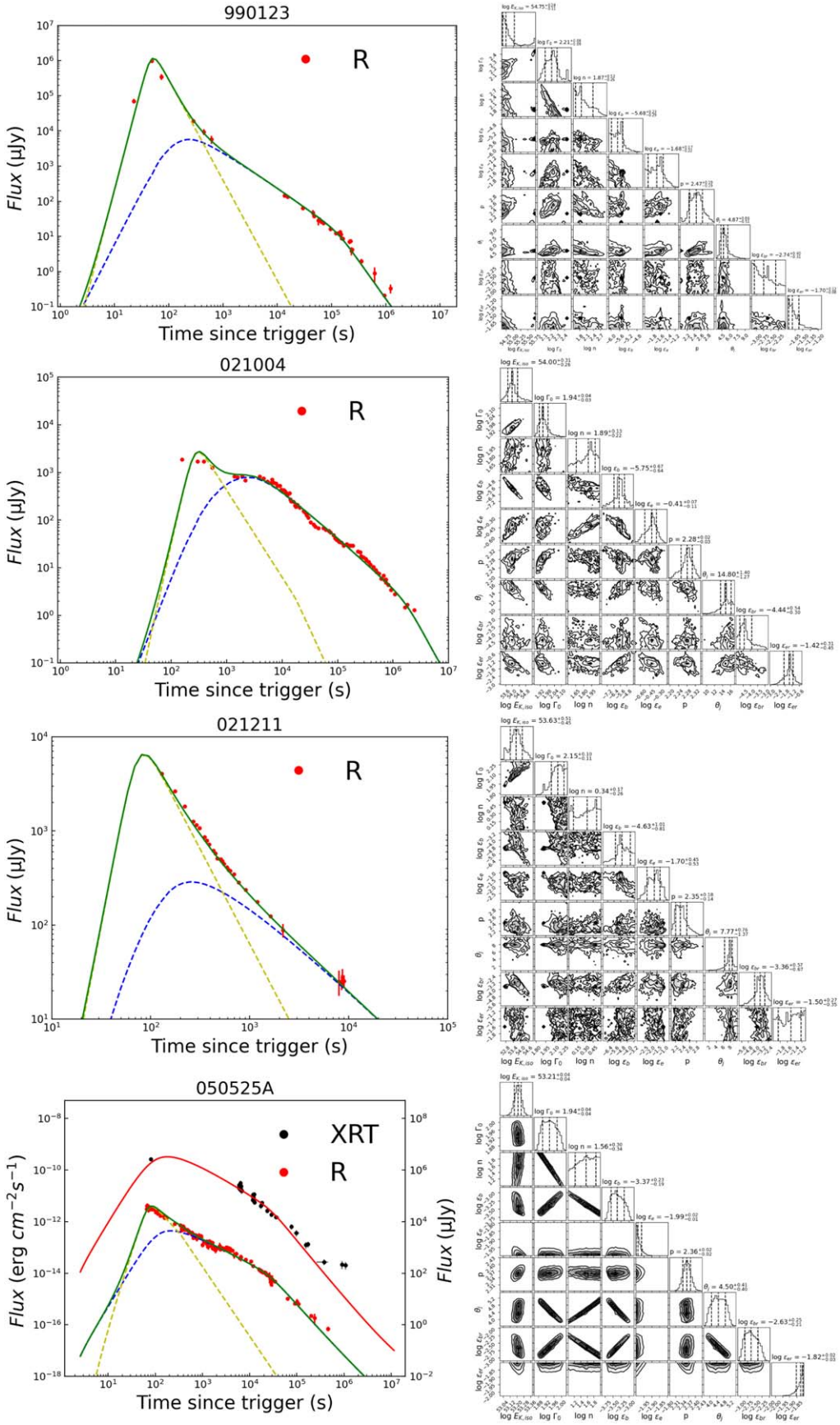

Figure 7. Similar to Figure 6, but for the LGRB sample.

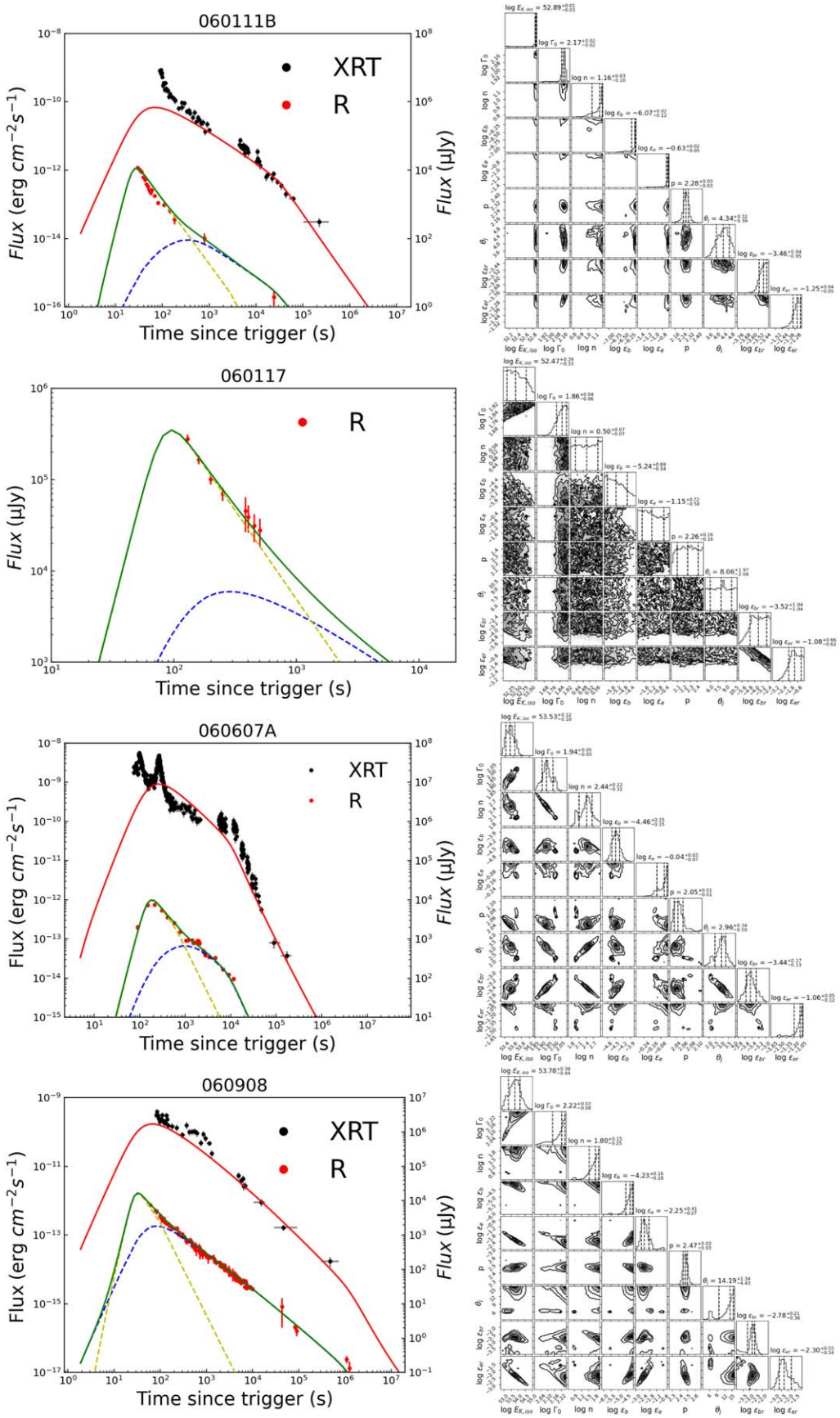

Figure 7. (Continued.)

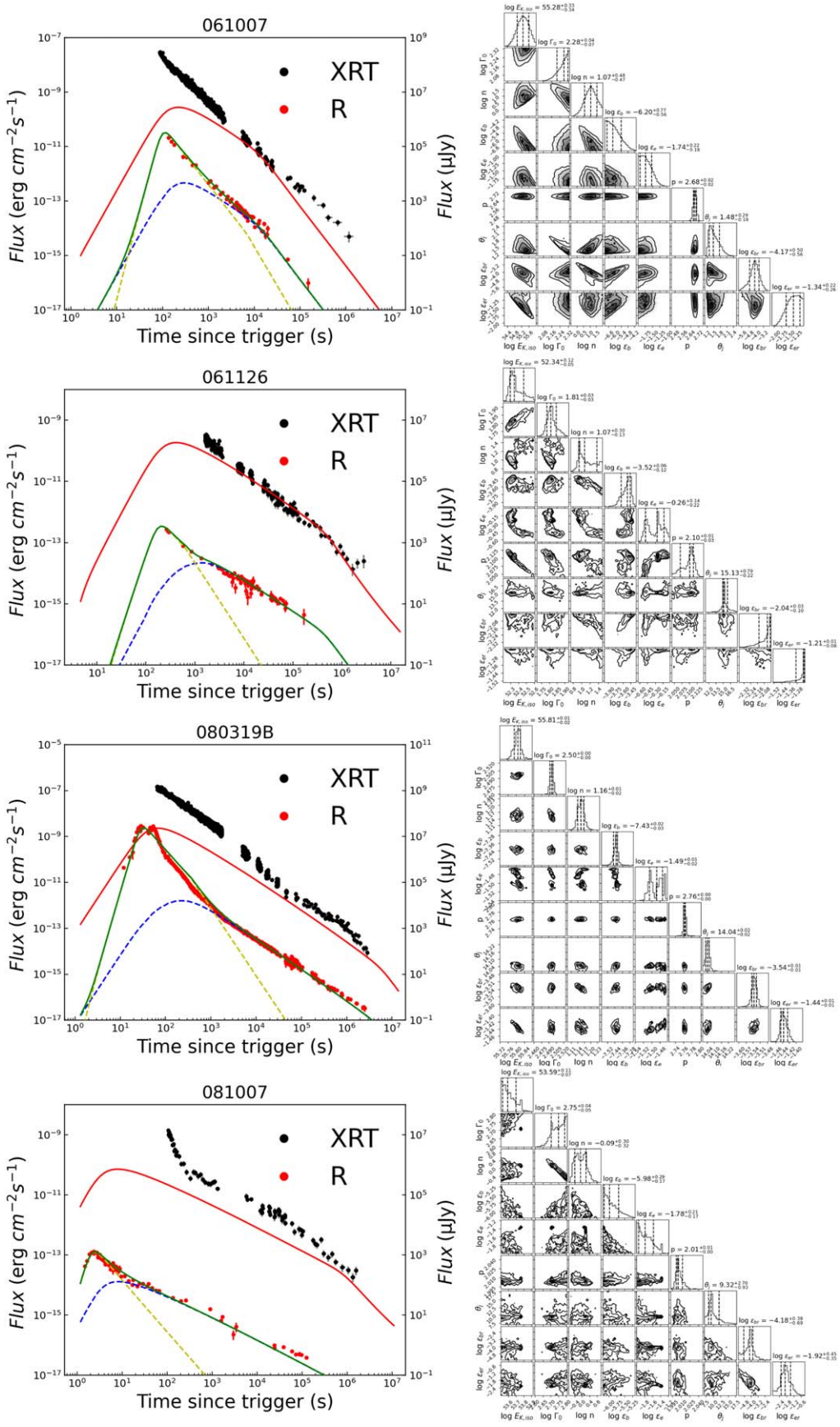

Figure 7. (Continued.)

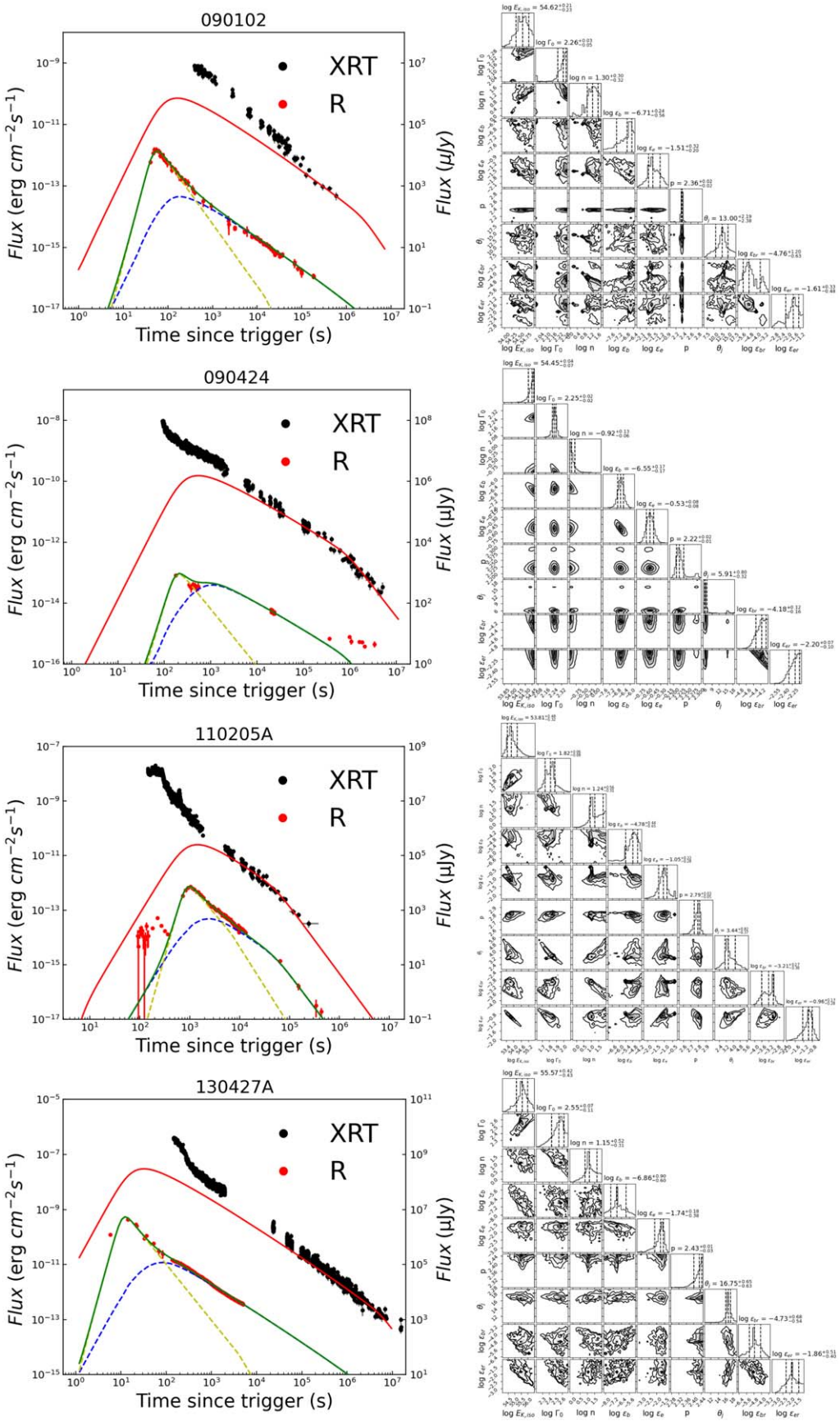

Figure 7. (Continued.)

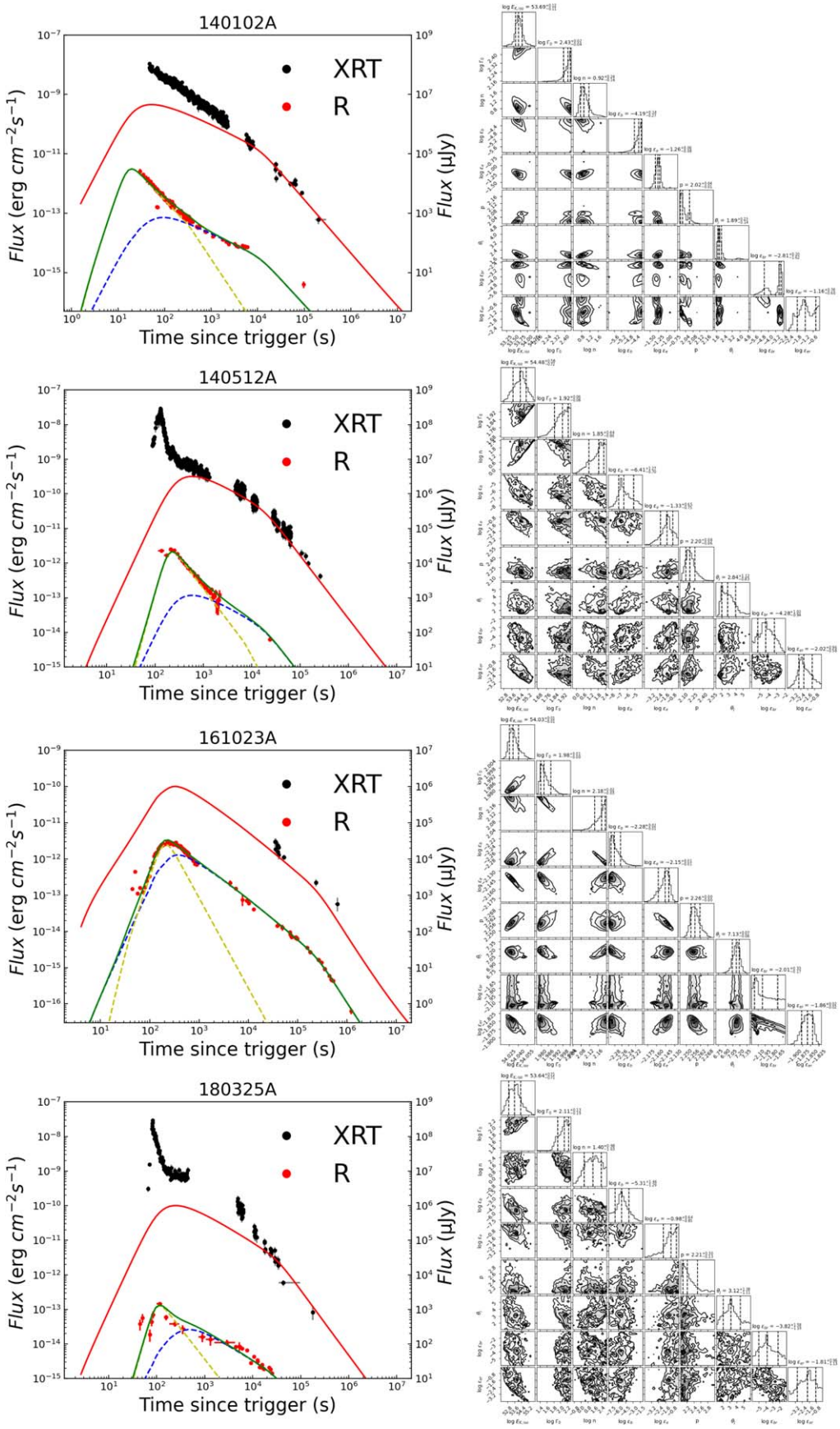

Figure 7. (Continued.)

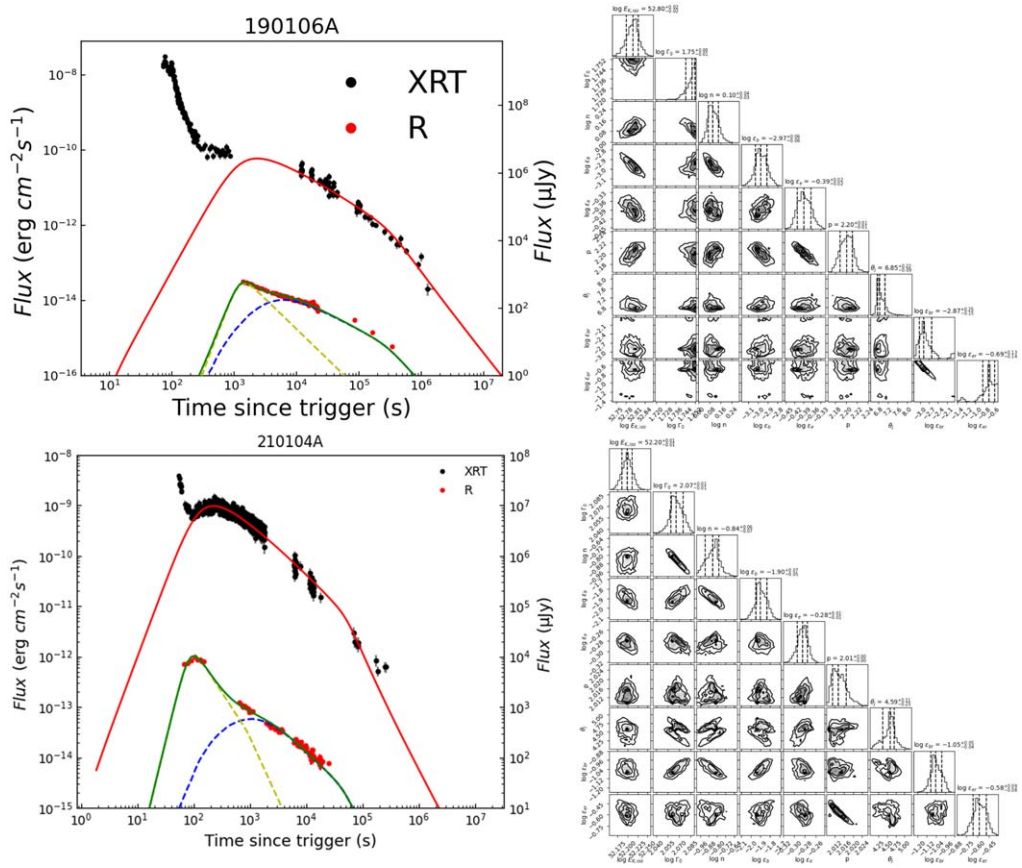

Figure 7. (Continued.)

GRB 161023A, the very early-optical light curve is characterized by optical flickering simultaneous with the gamma-ray emission (Gendre et al. 2012; Zheng et al. 2012; de Ugarte Postigo et al. 2018). For GRB 180325A, optical observations show an earlier flare, lasting about 10 s, which is not associated with the high-energy emission and is possibly the result of an RS. Observations of fluctuations in the optical RS emission are atypical and might be the result of density or velocity fluctuations in the material crossing the RS (Becerra et al. 2021).

3.3. Comparison and Analysis of GRBs with RS

With the parameters obtained from the above fitting, we can statistically analyze and compare the results. We first compared the properties of GRB 180418A with a sample of SGRBs (listed in Table 2) but did not find any universal features of their parameters. For SGRBs, the fitting parameters obtained by the MCMC algorithm span a narrower range compared with the LGRBs. Especially for the magnetization parameter R_B, the value for SGRBs is relatively low, indicating that RS signatures are not obvious compared with LGRBs. The reason the range for SGRB parameters is narrower than for LGRBs may be that the sample of SGRBs is far smaller than that of LGRBs. Combining SGRBs and LGRBs with RS emission, we further performed a series of statistical analyses of model parameters. Figure 8 shows parameter histogram distributions of RS and FS models for our sample. The following interesting analysis and conclusions can be drawn.

1. $E_{k,\rm iso}$: Wang et al. (2015) found that the typical isotropic kinetic energy is $10^{53.29\pm0.45}$ erg at the deceleration time. The isotropic kinetic energy $E_{k,\rm iso}$ of LGRBs is in the range 10^{52}–10^{55} erg; and the average value of its distribution is $10^{53.86}$ erg. Our statistical results for $E_{k,\rm iso}$ of LGRBs are consistent with those of Wang et al. (2015). The $E_{k,\rm iso}$ of SGRBs is in the range 10^{52}–10^{54} erg, with a mean value of $\sim10^{53.04}$ erg. The $E_{k,\rm iso}$ of GRB 180418A is $\sim10^{52.09}$ erg, on the low side among GRBs showing RS emission.
2. Γ_0: The initial fireball Lorentz factor for RS GRBs lies in the range $10^{1.6}$–$10^{2.8}$, and the peak distribution of Γ_0 is between $\sim10^{1.8}$ and $10^{2.0}$. Similarly, Japelj et al. (2014) found that Γ_0 lies between a few tens and ~600 for GRBs that exhibit RS emission.
3. Medium density n: The mean value of n for RS emission in GRBs is $\sim10^{1.04}$ cm^{-3}, consistent with other GRBs (e.g., Panaitescu & Kumar 2001b, 2002; Yi et al. 2020). Japelj et al. (2014) examined statistics of the ISM density n for their GRB samples with RS emission; their values for each GRB, obtained with different models, are spread over several orders of magnitude and were found to be as high as 10^4 cm^{-3}. This means that the burst environment of GRBs with RS emission does not differ significantly from that of the general GRB population.
4. $\varepsilon_{B,f}$ and $\varepsilon_{B,r}$: The fraction of internal energy to the magnetic field is $\varepsilon_{B,f}$ in the FS region and $\varepsilon_{B,r}$ in the RS region. The mean values of $\varepsilon_{B,f}$ and $\varepsilon_{B,r}$ are $10^{-4.93}$ and $10^{-3.27}$, respectively. Earlier modeling derived ε_B to be in the range of $10^{-2}-10^{-3}$ (Panaitescu & Kumar 2001b, 2002), and

Table 3
Fitting Results of External Shock Model for LGRBs

GRB[a]	$\log_{10}(E_{k,\rm iso}/{\rm erg})$	$\log\Gamma_0$	$\log_{10}(n/{\rm cm}^{-3})$	$\log\epsilon_{B,f}$	$\log\epsilon_{e,f}$	p	$\theta_{\rm j}$ (°)	$\log\epsilon_{B,r}$	$\log\epsilon_{e,r}$	z[b]	$R_B\equiv\varepsilon_{B,r}/\varepsilon_{B,f}$	$R_e\equiv\varepsilon_{\rm e,r}/\varepsilon_{e,f}$	$\chi^2_{\rm dof}$
990123	$54.75^{+0.28}_{-0.11}$	$2.21^{+0.08}_{-0.09}$	$1.87^{+0.52}_{-0.26}$	$-5.68^{+0.23}_{-0.29}$	$-1.68^{+0.17}_{-0.22}$	$2.47^{+0.19}_{-0.19}$	$4.87^{+0.86}_{-0.51}$	$-2.74^{+0.40}_{-0.31}$	$-1.70^{+0.12}_{-0.08}$	1.6	870.96	0.95	2.64
021004	$54.00^{+0.31}_{-0.26}$	$1.94^{+0.04}_{-0.03}$	$1.89^{+0.13}_{-0.22}$	$-5.75^{+0.67}_{-0.63}$	$-0.41^{+0.07}_{-0.11}$	$2.28^{+0.02}_{-0.03}$	$14.80^{+1.40}_{-1.27}$	$-4.44^{+0.54}_{-0.30}$	$-1.42^{+0.31}_{-0.45}$	2.329	20.42	0.10	3.45
021211	$53.63^{+0.51}_{-0.45}$	$2.15^{+0.10}_{-0.11}$	$1.34^{+0.17}_{-0.26}$	$-4.63^{+1.01}_{-0.81}$	$-1.70^{+0.45}_{-0.53}$	$2.35^{+0.18}_{-0.14}$	$7.77^{+0.76}_{-1.37}$	$-3.36^{+0.57}_{-0.67}$	$-1.50^{+0.27}_{-0.35}$	1.004	18.62	1.58	8.15
050525A	$53.21^{+0.04}_{-0.04}$	$1.94^{+0.04}_{-0.04}$	$1.56^{+0.30}_{-0.34}$	$-3.37^{+0.23}_{-0.19}$	$-1.99^{+0.02}_{-0.01}$	$2.36^{+0.02}_{-0.02}$	$4.50^{+0.41}_{-0.40}$	$-2.63^{+0.25}_{-0.21}$	$-1.82^{+0.02}_{-0.03}$	0.606	5.50	1.48	1.99
060111B	$52.89^{+0.01}_{-0.03}$	$2.17^{+0.02}_{-0.02}$	$1.16^{+0.03}_{-0.10}$	$-6.07^{+0.02}_{-0.12}$	$-0.63^{+0.02}_{-0.05}$	$2.28^{+0.03}_{-0.03}$	$4.34^{+0.32}_{-0.39}$	$-3.46^{+0.04}_{-0.05}$	$-1.25^{+0.04}_{-0.05}$	1.0	407.38	0.24	3.26
060117	$52.47^{+0.39}_{-0.33}$	$1.86^{+0.04}_{-0.06}$	$0.50^{+0.07}_{-0.07}$	$-5.24^{+0.69}_{-0.54}$	$-1.15^{+0.77}_{-0.58}$	$2.26^{+0.16}_{-0.16}$	$8.06^{+1.97}_{-2.08}$	$-3.52^{+1.04}_{-1.04}$	$-1.08^{+0.66}_{-0.62}$	0.042	52.48	1.17	0.22
060607A	$53.53^{+0.12}_{-0.10}$	$1.94^{+0.05}_{-0.03}$	$2.44^{+0.22}_{-0.32}$	$-4.46^{+0.15}_{-0.15}$	$-0.04^{+0.03}_{-0.07}$	$2.05^{+0.01}_{-0.01}$	$2.96^{+0.34}_{-0.50}$	$-3.44^{+0.17}_{-0.12}$	$-1.06^{+0.05}_{-0.12}$	3.082	10.47	0.10	4.38
060908	$53.78^{+0.38}_{-0.44}$	$2.22^{+0.03}_{-0.08}$	$1.80^{+0.15}_{-0.25}$	$-4.23^{+0.16}_{-0.28}$	$-2.25^{+0.41}_{-0.27}$	$2.47^{+0.03}_{-0.03}$	$14.19^{+1.34}_{-4.43}$	$-2.78^{+0.21}_{-0.36}$	$-2.30^{+0.55}_{-0.34}$	1.62	28.18	0.89	0.85
061007	$55.28^{+0.33}_{-0.34}$	$2.28^{+0.04}_{-0.07}$	$1.07^{+0.48}_{-0.47}$	$-6.20^{+0.77}_{-0.56}$	$-1.74^{+0.22}_{-0.18}$	$2.68^{+0.02}_{-0.02}$	$1.48^{+0.29}_{-0.18}$	$-4.17^{+0.50}_{-0.56}$	$-1.34^{+0.22}_{-0.26}$	1.261	107.15	0.68	2.29
061126	$52.34^{+0.12}_{-0.05}$	$1.81^{+0.03}_{-0.03}$	$1.07^{+0.30}_{-0.13}$	$-3.52^{+0.06}_{-0.12}$	$-0.26^{+0.14}_{-0.22}$	$2.10^{+0.01}_{-0.03}$	$15.13^{+0.79}_{-0.22}$	$-2.04^{+0.03}_{-0.10}$	$-1.21^{+0.01}_{-0.08}$	1.1588	30.20	0.11	1.26
080319B	$55.81^{+0.01}_{-0.02}$	$2.50^{+0.00}_{-0.00}$	$1.16^{+0.01}_{-0.02}$	$-7.43^{+0.02}_{-0.03}$	$-1.49^{+0.01}_{-0.02}$	$2.76^{+0.00}_{-0.00}$	$14.04^{+0.02}_{-0.02}$	$-3.54^{+0.01}_{-0.01}$	$-1.44^{+0.01}_{-0.01}$	0.937	7762.47	1.12	4.90
081007	$53.59^{+0.11}_{-0.07}$	$2.75^{+0.04}_{-0.05}$	$0.09^{+0.30}_{-0.32}$	$-5.98^{+0.29}_{-0.17}$	$-1.78^{+0.21}_{-0.17}$	$2.01^{+0.01}_{-0.00}$	$9.32^{+2.70}_{-0.93}$	$-4.18^{+0.38}_{-0.69}$	$-1.92^{+0.45}_{-0.35}$	0.5295	63.10	0.72	7.48
090102	$54.62^{+0.21}_{-0.23}$	$2.26^{+0.03}_{-0.05}$	$1.30^{+0.30}_{-0.32}$	$-6.71^{+0.24}_{-0.56}$	$-1.51^{+0.32}_{-0.20}$	$2.36^{+0.02}_{-0.02}$	$13.00^{+2.19}_{-2.38}$	$-4.76^{+1.20}_{-0.63}$	$-1.61^{+0.33}_{-0.48}$	1.547	89.13	0.79	2.87
090424	$54.45^{+0.04}_{-0.07}$	$2.25^{+0.02}_{-0.02}$	$0.92^{+0.13}_{-0.06}$	$-6.55^{+0.17}_{-0.17}$	$-0.53^{+0.08}_{-0.08}$	$2.22^{+0.02}_{-0.01}$	$5.91^{+0.80}_{-0.32}$	$-4.18^{+0.12}_{-0.16}$	$-2.20^{+0.07}_{-0.10}$	0.544	234.42	0.02	2.55
110205A	$53.81^{+0.48}_{-0.32}$	$1.82^{+0.06}_{-0.08}$	$1.24^{+0.56}_{-0.31}$	$-4.78^{+0.44}_{-0.65}$	$-1.05^{+0.22}_{-0.28}$	$2.79^{+0.03}_{-0.05}$	$3.44^{+0.82}_{-0.37}$	$-3.21^{+0.27}_{-0.38}$	$-0.96^{+0.17}_{-0.28}$	2.22	37.15	1.23	0.88
130427A	$55.57^{+0.42}_{-0.43}$	$2.55^{+0.07}_{-0.11}$	$1.15^{+0.52}_{-0.31}$	$-6.86^{+0.90}_{-0.60}$	$-1.74^{+0.18}_{-0.38}$	$2.43^{+0.01}_{-0.03}$	$16.75^{+0.65}_{-0.63}$	$-4.73^{+0.68}_{-0.54}$	$-1.86^{+0.51}_{-0.40}$	0.34	3890.45	0.14	4.52
140102A	$53.69^{+0.12}_{-0.11}$	$1.43^{+0.02}_{-0.04}$	$0.92^{+0.24}_{-0.16}$	$-4.19^{+1.27}_{-0.27}$	$-1.26^{+0.06}_{-0.08}$	$2.02^{+0.04}_{-0.01}$	$1.89^{+0.23}_{-0.14}$	$-2.81^{+0.20}_{-1.62}$	$-1.16^{+0.78}_{-0.60}$	2.02	23.99	1.26	4.98
140512A	$54.48^{+0.58}_{-0.72}$	$1.92^{+0.06}_{-0.08}$	$1.85^{+0.44}_{-0.80}$	$-6.41^{+1.27}_{-0.70}$	$-1.33^{+0.65}_{-0.75}$	$2.20^{+0.08}_{-0.06}$	$2.84^{+1.12}_{-0.83}$	$-4.28^{+1.02}_{-0.94}$	$-2.02^{+0.96}_{-0.58}$	0.725	134.90	0.20	0.9
161023A	$54.03^{+0.01}_{-0.01}$	$1.98^{+0.01}_{-0.00}$	$2.18^{+0.02}_{-0.03}$	$-2.28^{+0.02}_{-0.01}$	$-2.15^{+0.01}_{-0.01}$	$2.26^{+0.00}_{-0.00}$	$7.13^{+0.07}_{-0.08}$	$-2.01^{+0.33}_{-0.17}$	$-1.86^{+0.02}_{-0.02}$	2.71	1.86	1.95	12.43
180325A	$53.63^{+0.71}_{-0.71}$	$2.11^{+0.13}_{-0.19}$	$1.40^{+0.98}_{-1.03}$	$-5.31^{+1.46}_{-1.29}$	$-0.98^{+0.64}_{-0.85}$	$2.21^{+0.30}_{-0.13}$	$3.12^{+1.38}_{-1.11}$	$-3.82^{+1.58}_{-1.19}$	$-1.81^{+0.96}_{-1.13}$	2.25	30.90	0.15	1.96
190106A	$52.80^{+0.02}_{-0.02}$	$1.75^{+0.00}_{-0.09}$	$0.10^{+0.04}_{-0.03}$	$-2.97^{+0.06}_{-0.06}$	$-0.39^{+0.02}_{-0.02}$	$2.20^{+0.01}_{-0.01}$	$6.85^{+0.22}_{-0.09}$	$-2.87^{+0.25}_{-0.15}$	$-0.69^{+0.13}_{-0.14}$	1.861	1.26	0.50	1.42
210104A	$52.20^{+0.01}_{-0.01}$	$2.07^{+0.01}_{-0.01}$	$0.84^{+0.06}_{-0.07}$	$-1.90^{+0.01}_{-0.01}$	$-0.28^{+0.01}_{-0.01}$	$2.01^{+0.00}_{-0.00}$	$4.59^{+0.11}_{-0.23}$	$-1.05^{+0.05}_{-0.44}$	$-0.58^{+0.09}_{-0.08}$	0.46	7.08	0.50	0.90

Notes.

[a] Optical light-curve data references. GRB 990123: Castro-Tirado et al. (1999). GRB 021004: Mirabal et al. (2003). GRB 021211: Vreeswijk et al. (2003). GRB 050525A: Blustin et al. (2006). GRB 060111B: Stratta et al. (2009). GRB 060117: Jelínek et al. (2006). GRB 060607A: Nysewander et al. (2009). GRB 060908: Covino et al. (2010). GRB 061007: Mundell et al. (2007). GRB 061126: Gomboc et al. (2008). GRB 080319B: Bloom et al. (2009). GRB 081007: Jin et al. (2013). GRB 090102: Gendre et al. (2010). GRB 090424: Kann et al. (2010). GRB 110205A: Gendre et al. (2012). Virgili et al. (2013). GRB 130427A: Vestrand et al. (2014). GRB 140102A: Gupta et al. (2021). GRB 140512A: Huang et al. (2016). GRB 161023A: de Ugarte Postigo et al. (2018). GRB 180325A: Becerra et al. (2021). GRB 190106A: Zhu et al. (2023). GRB 210204A: Zhang et al. (2022).

[b] Redshift references. GRB 990123: Blandford & Helfand (1999). GRB 021004: Fox et al. (2008). GRB 021211: Li et al. (2003). GRB 050525A: Foley et al. (2005).GRB 060111B: Stratta et al. (2009). GRB 060117: Tanvir (2006). GRB 060607A: Nysewander et al. (2009). GRB 060908: Morgan (2006). GRB 061007: Mundell et al. (2007). GRB 061126: Gomboc et al. (2008). GRB 080319B: Vreeswijk et al. (2008). GRB 081007: Berger et al. (2008). GRB 090102: de Ugarte Postigo et al. (2009). GRB 090424: Chornock et al. (2009). GRB 110205A: Gendre et al. (2012). GRB 130427A: Levan et al. (2013). GRB 140102A: Gupta et al. (2021). GRB 140512A: Huang et al. (2016). GRB 161023A: de Ugarte Postigo et al. (2018). GRB 180325A: Heintz et al. (2018). GRB 190106A: Zhu et al. (2023). GRB 210204A: Zhang et al. (2022). The redshift of GRB 060111B is unknown; thus, it is set to the typical value of 1.0.

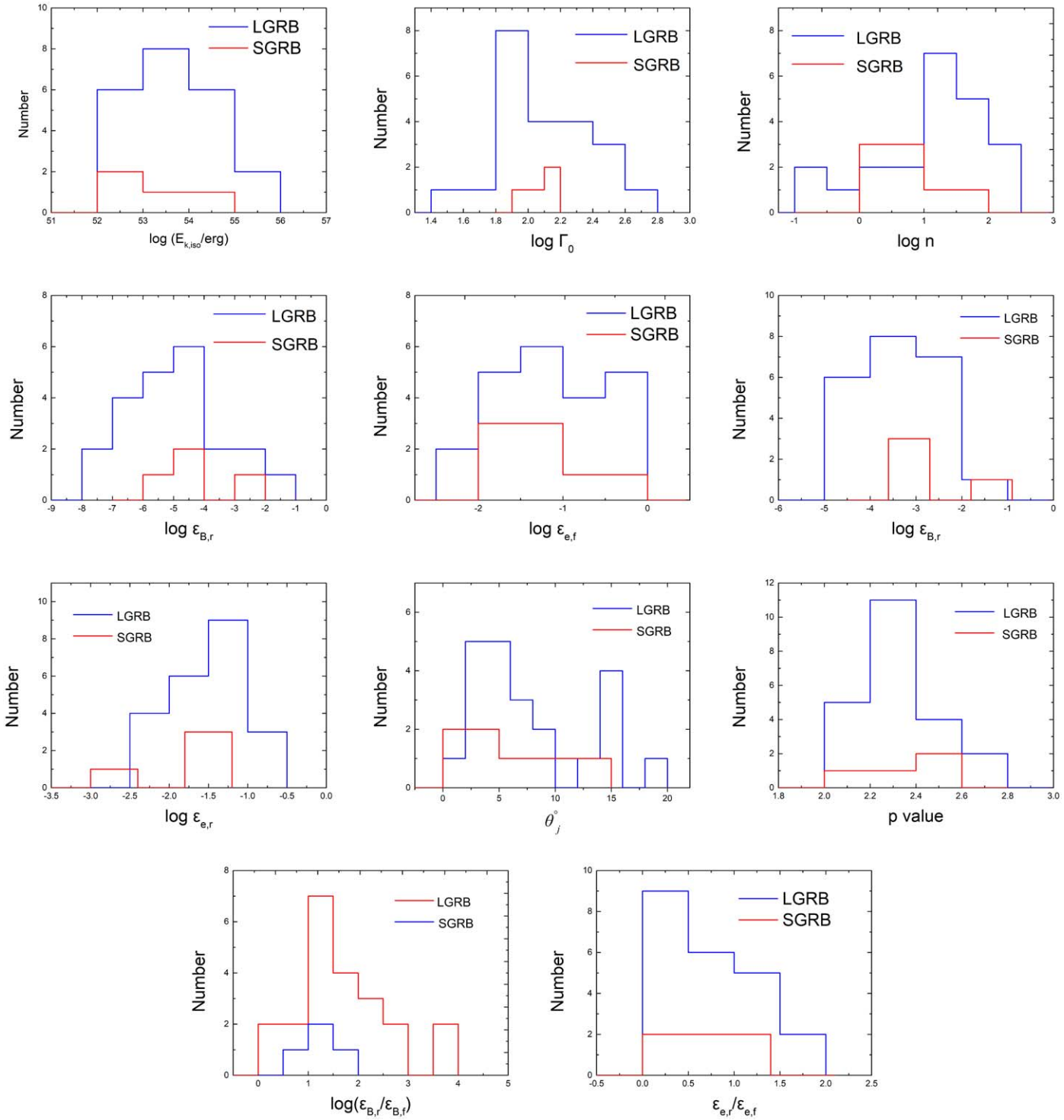

Figure 8. Parameter distributions of RS and FS models for GRBs.

later studies showed that ε_B can be as low as 10^{-6} (e.g., Kumar & Barniol Duran 2009; Santana et al. 2014; Wang et al. 2015). Japelj et al. (2014) computed statistics of $\varepsilon_{B,f}$, but were unable to test whether the derived $\varepsilon_{B,f}$ in afterglows with prominent RS components is generally lower than in non-RS events. Our statistical results show that it may have a larger parameter range, and in the FS region, ε_B is lower for GRBs with RS emission.

5. $\varepsilon_{e,f}$ and $\varepsilon_{e,r}$: The fractions of internal energy to the electrons field are $\varepsilon_{e,f}$ in the FS region and $\varepsilon_{e,r}$ in the RS region. The mean values of $\varepsilon_{e,f}$ and $\varepsilon_{e,r}$ are $10^{-1.17}$ and $10^{-1.55}$, respectively. From individual modeling, the preferred ε_e value is $\sim$0.1 (Wijers & Galama 1999; Panaitescu & Kumar 2001b, 2002). However, a morphological study of early-time optical light curves suggests a preferred value of 0.01 (Gao et al. 2015). Our results imply that $\varepsilon_{e,f}$ of GRBs with RS emission may be more consistent with Gao et al. (2015).
6. R_B: We calculated the ratio $R_B \equiv \varepsilon_{B,r}/\varepsilon_{B,f}$ of SGRBs and LGRBs. One can see that most of the values lie in the

range 0–100, but there are some GRBs with higher values (GRB 990123, GRB 080319B, GRB 130427A). A morphological study of early-time optical light curves suggests a preferred value of 100 (Gao et al. 2015), which means that our statistical results are in agreement with those of the morphological study by Gao et al. (2015). The R_B values of SGRBs are generally similar to those of LGRBs.

7. R_e: We also calculated the ratio $R_e \equiv \varepsilon_{e,r}/\varepsilon_{e,f}$, with the mean value of R_e is 0.71. We can see that most of its values lie in the range 0–1.0, implying that GRB shows RS emission. The R_e values of SGRBs are also generally similar to those of LGRBs. The radiation efficiency of the RS is lower than that of the FS.
8. p: The electron power-law index p, even though it has a distribution peaking at the theoretically predicted value (2.2–2.3), can vary from being smaller than 2 to above 3. The derived p values from the afterglow data of Swift GRBs and their best Gaussian fits have a typical value of 2.33 (Wang et al. 2015). We find that the mean value of p for RS emission GRBs is 2.32, consistent with previous results (e.g., Wang et al. 2015). On the other hand, our p values exhibit a wide range for GRBs with RS.
9. Jet opening angle θ_j: For the distribution of θ_j, the mean value is 7.°53. From the jet-break sample, Wang et al. (2015) derived the typical jet opening angle to be 2.°5. Most of our θ_j fitting results exceed 2.°5, which may be because there are no obvious jet breaks in the late epochs of light curves of GRBs showing RS emission.

4. Conclusions

In this work we have reported our early-time optical observations of GRB 180418A, and analyzed its multiwavelength data together with Swift data. We also presented a detailed study of a group of three SGRB and 22 LGRB afterglows that show RS signatures in early-optical light curves.

Our comparison and analysis show that the parameters of LGRBs are in a relatively wide range, while the parameters of SGRBs are limited to a relatively small range. GRB 180418A is basically consistent with the other three SGRBs, implying that GRB 180418A may belong to the category of short bursts. We also find that most of the model parameters of SGRBs are not very special compared with LGRBs.

Strong RS emission is produced when the GRB outflow is baryonic, only mildly magnetized. In order to produce an RS afterglow that can outshine the FS emission (RS II light curve), a magnetization parameter of $R_B > 1$ is required (Zhang & Kobayashi 2005). Our RS sample fitting results show that a low typical value of $\varepsilon_{B,f}$ does exist; the presence of strong RS emission (compared with FS emission) requires $\varepsilon_{B,f} < \varepsilon_{B,r}$ (i.e., high R_B). The R_B values of SGRBs are generally small, indicating that the RS signal is not prominent. This could be one of the reasons for the lack of SGRBs showing RS emission.

The FS peak, given a low R_B ratio, is likely to occur when the RS afterglow component is still very bright, and this could explain the lack of RS I light curves (Japelj et al. 2014). The LGRBs we collected are dominated by RS II light curves, which also supports this view.

It is worth noting that the results in this paper are solely based on fitting the current small observational sample. To better study the nature of RS emission and to determine the origin of RS suppression, it is clear that larger samples of confirmed RS components (especially SGRBs with RS emission) are vital. A future dedicated facility with rapid-response ability and a wide field of view could help with these issues, and this is a key element in the Chinese–French mission SVOM, the Ground Wide Angle Cameras (Paul et al. 2011).

Acknowledgments

This work is supported by the National Natural Science Foundation of China (Nos. 12373042, U1938201, 12133003), and Bagui Scholars Programme.

A.V.F.'s group at U.C. Berkeley is grateful for financial assistance from the Christopher R. Redlich Fund, Alan Eustace (W.Z. is a Eustace Specialist in Astronomy), and many other donors. KAIT and its ongoing operation were made possible by donations from Sun Microsystems, Inc., the Hewlett-Packard Company, AutoScope Corporation, Lick Observatory, the U.S. NSF, the University of California, the Sylvia & Jim Katzman Foundation, and the TABASGO Foundation. Research at Lick Observatory is partially supported by a generous gift from Google.

ORCID iDs

Xiang-Gao Wang https://orcid.org/0000-0001-8411-8011
Zi-Min Zhou https://orcid.org/0000-0003-3360-2211
WeiKang Zheng https://orcid.org/0000-0002-2636-6508
Shuang-Xi Yi https://orcid.org/0000-0003-0672-5646
Liang-Jun Chen https://orcid.org/0009-0007-7188-3196
Da-Bin Lin https://orcid.org/0000-0003-1474-293X
En-Wei Liang https://orcid.org/0000-0002-7044-733X
Alexei V. Filippenko https://orcid.org/0000-0003-3460-0103

References

Abbott, B. P., Abbott, R., Abbott, T. D., et al. 2017, ApJL, 848, L13
Akerlof, C., Balsano, R., Barthelmy, S., et al. 1999, Natur, 398, 400
Amati, L., Frontera, F., Tavani, M., et al. 2002, A&A, 390, 81
Arnaud, K. A. 1996, in ASP Conf. Ser. 101, Astronomical Data Analysis Software and Systems V ed. G. H. Jacoby & J. Barnes (San Francisco, CA: ASP), 17
Becerra, R. L., Dichiara, S., Watson, A. M., et al. 2019, ApJ, 881, 12
Becerra, R. L., De Colle, F., Cantó, J., et al. 2021, ApJ, 908, 39
Beniamini, P., Nava, L., & Piran, T. 2016, MNRAS, 461, 51
Berger, E., Fox, D. B., Cucchiara, A., & Cenko, S. B. 2008, GCN, 8335, 1
Bissaldi, E., & Veres, P. 2018, GCN, 22656, 1
Blandford, R. D., & Helfand, D. J. 1999, MNRAS, 305, L45
Bloom, J. S., Perley, D. A., Li, W., et al. 2009, ApJ, 691, 723
Blustin, A. J., Band, D., Barthelmy, S., et al. 2006, ApJ, 637, 901
Bright, J., Mooley, K. P., & Fender, R. P. 2018, GCN, 22697, 1
Cano, Z. 2013, MNRAS, 434, 1098
Castro-Tirado, A. J., Zapatero-Osorio, M. R., Caon, N., et al. 1999, Sci, 283, 2069
Choi, C., Kim, Y., Park, W., Shin, S., & Im, M. 2018, GCN, 22668, 1
Chornock, R., Perley, D. A., Cenko, S. B., & Bloom, J. S. 2009, GCN, 9243, 1
Covino, S., Campana, S., Conciatore, M. L., et al. 2010, A&A, 521, A53
D'Agostini, G. 2005, arXiv:physics/0511182
de Ugarte Postigo, A., Jakobsson, P., Malesani, D., et al. 2009, GCN, 8766, 1
de Ugarte Postigo, A., Thöne, C. C., Bolmer, J., et al. 2018, A&A, 620, A119
D'Elia, V., D'Ai, A., Evans, P. A., et al. 2018, GCN, 22646, 1
Eichler, D., Livio, M., Piran, T., & Schramm, D. N. 1989, Natur, 340, 126
Evans, P. A., Beardmore, A. P., Page, K. L., et al. 2009, MNRAS, 397, 1177
Fan, Y., & Piran, T. 2006, MNRAS, 369, 197
Fan, Y.-Z., Dai, Z.-G., Huang, Y.-F., & Lu, T. 2002, ChJAA, 2, 449
Fan, Y. Z., Wei, D. M., & Wang, C. F. 2004, A&A, 424, 477
Filippenko, A. V., Li, W. D., Treffers, R. R., & Modjaz, M. 2001, IAU Colloq. 183, Small-Telescope Astronomy on Global Scales (Cambridge: Cambridge Univ. Press), 121

Foley, R. J., Chen, H. W., Bloom, J., & Prochaska, J. X. 2005, GCN, 3483, 1
Fong, W., Tanvir, N. R., Levan, A. J., & Chornock, R. 2018, GCN, 22659, 1
Foreman-Mackey, D., Hogg, D. W., Lang, D., & Goodman, J. 2013, PASP, 125, 306
Fox, A. J., Ledoux, C., Vreeswijk, P. M., Smette, A., & Jaunsen, A. O. 2008, A&A, 491, 189
Fraija, N. 2014, MNRAS, 437, 2187
Fraija, N., Dichiara, S., Pedreira, A. C. C. D. E. S., et al. 2019, ApJL, 879, L26
Fraija, N., Lee, W., & Veres, P. 2016, ApJ, 818, 190
Gao, H., Wang, X.-G., Mészáros, P., & Zhang, B. 2015, ApJ, 810, 160
Gendre, B., Klotz, A., Palazzi, E., et al. 2010, MNRAS, 405, 2372
Gendre, B., Atteia, J. L., Boër, M., et al. 2012, ApJ, 748, 59
Giacomazzo, B., Rezzolla, L., & Baiotti, L. 2011, PhRvD, 83, 044014
Gomboc, A., Kobayashi, S., Guidorzi, C., et al. 2008, ApJ, 687, 443
Gomboc, A., Kobayashi, S., Mundell, C. G., et al. 2009, in AIP Conf. Ser. 1133, Gamm-Ray Burst, ed. C. Meegan, C. Kouveliotou, & N. Gehrels (Melville, NY: AIP), 145
Granot, J., & Sari, R. 2002, ApJ, 568, 820
Guidorzi, C., Martone, R., Kobayashi, S., et al. 2018, GCN, 22648, 1
Gupta, R., Oates, S. R., Pandey, S. B., et al. 2021, MNRAS, 505, 4086
Harrison, R., & Kobayashi, S. 2013, ApJ, 772, 101
Heintz, K. E., Fynbo, J. P. U., & Malesani, D. 2018, GCN, 22535, 1
Hjorth, J., Sollerman, J., Møller, P., et al. 2003, Natur, 423, 847
Horiuchi, T., Hanayama, H., Honma, M., et al. 2018, GCN, 22670, 1
Huang, X.-L., Xin, L.-P., Yi, S.-X., et al. 2016, ApJ, 833, 100
Huang, Y. F., Gou, L. J., Dai, Z. G., & Lu, T. 2000, ApJ, 543, 90
Ivezić, Ž, Connolly, A. J., VanderPlas, J. T., & Gray, A. 2014, Statistics, Data Mining, and Machine Learning in Astronomy (Princeton, NJ: Princeton Univ. Press)
Japelj, J., Kopač, D., Kobayashi, S., et al. 2014, ApJ, 785, 84
Jelínek, M., Prouza, M., Kubánek, P., et al. 2006, A&A, 454, L119
Jin, Z.-P., Covino, S., Della Valle, M., et al. 2013, ApJ, 774, 114
Kann, D. A., Klose, S., Zhang, B., et al. 2010, ApJ, 720, 1513
Klotz, A., Atteia, J. L., Boer, M., Eymar, L., & Gendre, B. 2018, GCN, 22671, 1
Kobayashi, S., & Zhang, B. 2003, ApJL, 582, L75
Kouveliotou, C., Meegan, C. A., Fishman, G. J., et al. 1993, ApJL, 413, L101
Kumar, A., Pandey, S. B., Gupta, R., et al. 2021, GCN, 29421, 1
Kumar, P., & Barniol Duran, R. 2009, MNRAS, 400, L75
Kumar, P., & Panaitescu, A. 2003, MNRAS, 346, 905
Kumar, P., & Zhang, B. 2015, PhR, 561, 1
Lamb, G. P., Tanvir, N. R., Levan, A. J., et al. 2019, ApJ, 883, 48
Lee, W. H., & Ramirez-Ruiz, E. 2007, NJPh, 9, 17
Levan, A. J., Cenko, S. B., Perley, D. A., & Tanvir, N. R. 2013, GCN, 14455, 1
Levesque, E., Chornock, R., Kewley, L., et al. 2009, GCN, 9264, 1
Li, W., Filippenko, A. V., Chornock, R., & Jha, S. 2003, ApJL, 586, L9
Liang, E.-W., Racusin, J. L., Zhang, B., Zhang, B.-B., & Burrows, D. N. 2008, ApJ, 675, 528
Lien, A., Sakamoto, T., Barthelmy, S. D., et al. 2016, ApJ, 829, 7
Lloyd-Ronning, N. 2018, Galax, 6, 103
Lloyd-Ronning, N. M., & Fryer, C. L. 2017, MNRAS, 467, 3413
Lü, H.-J., Liang, E.-W., Zhang, B.-B., & Zhang, B. 2010, ApJ, 725, 1965
Malesani, D., Heintz, K. E., Stone, M., & Stone, J. 2018, GCN, 22660, 1
Meszaros, P., & Rees, M. J. 1993, ApJ, 405, 278
Mészáros, P., & Rees, M. J. 1997, ApJ, 476, 232
Mészáros, P., & Rees, M. J. 1999, MNRAS, 306, L39
Mirabal, N., Halpern, J. P., Chornock, R., et al. 2003, ApJ, 595, 935
Misra, K., Paswan, A., Singh, M., et al. 2018, GCN, 22663, 1
Morgan, A. N., vanden Berk, D. E., Brown, P., & Evans, P. A. 2006, GCN, 5553, 1
Mundell, C. G., Melandri, A., Guidorzi, C., et al. 2007, ApJ, 660, 489
Mundell, C. G., Kopač, D., Arnold, D. M., et al. 2013, Natur, 504, 119
Nakar, E., & Piran, T. 2004, MNRAS, 353, 647
Narayan, R., Paczynski, B., & Piran, T. 1992, ApJL, 395, L83
Nysewander, M., Reichart, D. E., Crain, J. A., et al. 2009, ApJ, 693, 1417
Osborne, J. P., Burrows, D. N., Kennea, J. A., et al. 2018, GCN, 22649, 1
Paciesas, W. S. & Fermi GBM Collaboration 2012, AAS Meeting Abstracts, 219, 149.12
Paczynski, B. 1991, AcA, 41, 257
Palmer, D. M., Barthelmy, S. D., Cummings, J. R., et al. 2018, GCN, 22658, 1
Panaitescu, A., & Kumar, P. 2001a, ApJ, 554, 667
Panaitescu, A., & Kumar, P. 2001b, ApJL, 560, L49
Panaitescu, A., & Kumar, P. 2002, ApJ, 571, 779
Paul, J., Wei, J., Basa, S., & Zhang, S.-N. 2011, CRPhy, 12, 298
Pei, Y. C. 1992, ApJ, 395, 130
Piran, T. 1999, PhR, 314, 575
Pozanenko, A., Elenin, L., Litvinenko, E., et al. 2013, in EAS Publications Ser. 61, Gamma-ray Bursts: 15 Years of GRB Afterglows, ed. A. J. Castro-Tirado, J. Gorosabel, & I. H. Park (Les Ulis: EDP Sciences), 259
Qin, Y., Liang, E.-W., Liang, Y.-F., et al. 2013, ApJ, 763, 15
Ren, J., Lin, D.-B., Zhang, L.-L., et al. 2019, ApJ, 885, 60
Roming, P. W. A., Vanden Berk, D., Pal'shin, V., et al. 2006, ApJ, 651, 985
Rosswog, S., & Ramirez-Ruiz, E. 2002, MNRAS, 336, L7
Rouco Escorial, A., Fong, W., Veres, P., et al. 2021, ApJ, 912, 95
Ruffert, M., & Janka, H. T. 1998, A&A, 338, 535
Sakamoto, T., Barthelmy, S. D., Barbier, L., et al. 2008, ApJS, 175, 179
Santana, R., Barniol Duran, R., & Kumar, P. 2014, ApJ, 785, 29
Sari, R., & Piran, T. 1999a, ApJ, 520, 641
Sari, R., & Piran, T. 1999b, ApJL, 517, L109
Sari, R., Piran, T., & Narayan, R. 1998, ApJL, 497, L17
Schady, P., & Chen, T. W. 2018, GCN, 22666, 1
Schlegel, D. J., Finkbeiner, D. P., & Davis, M. 1998, ApJ, 500, 525
Schulze, S., Klose, S., Björnsson, G., et al. 2011, A&A, 526, A23
Siegel, M. H., & Lien, A. Y. 2021, GCN, 29436, 1
Sota, A., Hu, Y., Tello, J. C., Carrasco, I., & Castro-Tirado, A. J. 2018, GCN, 22657, 1
Steele, I. A., Mundell, C. G., Smith, R. J., Kobayashi, S., & Guidorzi, C. 2009, Natur, 462, 767
Stratta, G., Pozanenko, A., Atteia, J. L., et al. 2009, A&A, 503, 783
Strausbaugh, R., & Cucchiara, A. 2021, GCN, 29431, 1
Sutaria, F., & Ray, A. 2021, GCN, 29759, 1
Tanvir, N. R. 2006, GCN, 4534, 1
Troja, E., Butler, N., Watson, A. M., et al. 2018a, GCN, 22652, 1
Troja, E., Butler, N., Watson, A. M., et al. 2018b, GCN, 22664, 1
Vestrand, W. T., Wren, J. A., Panaitescu, A., et al. 2014, Sci, 343, 38
Virgili, F. J., Mundell, C. G., Pal'shin, V., et al. 2013, ApJ, 778, 54
Vreeswijk, P., Fruchter, A., Hjorth, J., & Kouveliotou, C. 2003, GCN, 1785, 1
Vreeswijk, P. M., Milvang-Jensen, B., Smette, A., et al. 2008, GCN, 7451, 1
Wang, X.-G., Liang, E.-W., Li, L., et al. 2013, ApJ, 774, 132
Wang, X.-G., Zhang, B., Liang, E.-W., et al. 2018, ApJ, 859, 160
Wang, X.-G., Zhang, B., Liang, E.-W., et al. 2015, ApJS, 219, 9
Wang, X.-Y., Li, Z., Waxman, E., & Mészáros, P. 2007, ApJ, 664, 1026
Wijers, R. A. M. J., & Galama, T. J. 1999, ApJ, 523, 177
Woosley, S. E. 1993, ApJ, 405, 273
Wu, X. F., Dai, Z. G., Huang, Y. F., & Lu, T. 2005, ApJ, 619, 968
Xin, L.-P., Liang, E.-W., Wei, J.-Y., et al. 2011, MNRAS, 410, 27
Xin, L. P., Yan, J. Z., Wei, J. Y., et al. 2018, GCN, 22661, 1
Yang, J., Ai, S., Zhang, B.-B., et al. 2022, Natur, 612, 232
Yi, S.-X., Wu, X.-F., & Dai, Z.-G. 2013, ApJ, 776, 120
Yi, S.-X., Wu, X.-F., Zou, Y.-C., & Dai, Z.-G. 2020, ApJ, 895, 94
Yost, S. A., Harrison, F. A., Sari, R., & Frail, D. A. 2003, ApJ, 597, 459
Zhang, B., & Kobayashi, S. 2005, ApJ, 628, 315
Zhang, B., Kobayashi, S., & Mészáros, P. 2003, ApJ, 595, 950
Zhang, B., Liang, E., Gupta, N., et al. 2007a, RSPTA, 365, 1257
Zhang, B., Liang, E., Page, K. L., et al. 2007b, ApJ, 655, 989
Zhang, B., Zhang, B.-B., Virgili, F. J., et al. 2009, ApJ, 703, 1696
Zhang, B. B., Liu, Z. K., Peng, Z. K., et al. 2021, NatAs, 5, 911
Zhang, F.-W., Shao, L., Yan, J.-Z., & Wei, D.-M. 2012, ApJ, 750, 88
Zhang, L.-L., Xin, L.-P., Wang, J., et al. 2022, ApJ, 941, 63
Zhang, S., Jin, Z.-P., & Wei, D.-M. 2015, ApJ, 798, 3
Zheng, W., & Filippenko, A. V. 2018, GCN, 22647, 1
Zheng, W., Filippenko, A. V., & GRB Team, K. A. I. T. 2021, GCN, 29430, 1
Zheng, W., Shen, R. F., Sakamoto, T., et al. 2012, ApJ, 751, 90
Zhu, Z.-P., Xu, D., Fynbo, J. P. U., et al. 2023, ApJ, 948, 30
Zou, Y. C., Wu, X. F., & Dai, Z. G. 2005, MNRAS, 363, 93